

ALGORITHMS OF IMAGE PROCESSING AND X-RAY DIFFRACTION
ANALYSES FOR CHARACTERIZATION OF MAGNETIC NANOSTRUCTURES

A Thesis

Presented to

The Faculty of the Department of Physics and Astronomy
California State University, Los Angeles

In Partial Fulfillment

of the Requirements for the Degree

Master of Science

in

Physics

By

Vicente Pena Perez

May 2024

© 2024

Vicente Pena Perez

ALL RIGHTS RESERVED

The thesis of Vicente Pena Perez is approved.

Dr. Oscar Bernal, Thesis Director

Dr. Armen Kocharian Committee Member

Dr. Jose Rodriguez , Committee Member

Dr. Radi Jishi, Department Chair

California State University, Los Angeles

May 2024

ABSTRACT

Algorithms of Image Processing and X-Ray Diffraction Analyses for Characterization of Magnetic Nanostructures

By

Vicente Pena Perez

This research delves into the intricate world of magnetic nanostructures, focusing on their morphological properties and how these influence their magnetic behaviors. As the field of nanotechnology continues to expand, there is a growing need for precise and quantitative methods to characterize magnetic nanomaterials. Our project, conducted in collaboration with the research group at Cal State LA, introduces a novel algorithm designed to analyze Scanning Electron Microscopy (SEM) images and juxtapose these with Powdered X-ray Diffraction (PXRD) elemental analyses.

At the foundation of our approach are established filtration techniques, enhanced with the integration of node extraction and a groundbreaking reconnection algorithm driven by 2D Gaussian mapping. We aim to classify nanostructures based on size, differentiating between lengths for nanotubes and nanosheets, and radii for nanospheres. Our investigation further extends to exploring porosity, layer sizes, and the subsequent impact on magnetic properties. This comprehensive study covers a variety of synthesized core-shell nanoparticles, including metallic (Fe, Ni, Co) and metal-free phthalocyanine and porphyrin nanoparticles, all subjected to meticulous

characterization processes.

Magnetic properties are scrutinized using Physical Property Measurement System (PPMS) and Electron Paramagnetic Resonance (EPR), establishing a correlation between nanostructure layer design and magnetic characteristics. Through this research, we aim to provide a robust and innovative solution for the accurate and quantitative analysis of magnetic nanomaterials, contributing valuable insights to the field of nanotechnology and materials science.

ACKNOWLEDGMENTS

This work not only contributes to the existing body of knowledge on nanoparticle characterization but also showcases the synergy between computational analysis and experimental techniques. As we continue to push the boundaries of nanotechnology, it is the integration of such interdisciplinary approaches that will drive innovation and discovery in the field.

For this reason, I extend my deepest gratitude to Dr. Armen Kocharian, Dr. Oscar Bernal, Dr. Jose Rodriguez, and the entire research group, including Armond, Cristian, Franco, Erick, Sarah, Timothy, and Jonah, for their invaluable contributions to this research. Motivation and guidance were pivotal in initiating this work prior to my dissertation. The knowledge and experience acquired since Fall 2023 semester as a group has been immeasurable and instrumental in shaping this study.

I would like to extend special acknowledgment to the Center for Advancement Toward Sustainable Urban Systems (NSF CREST CATSUS), where I was honored to receive a fellowship. This award greatly aided in surmounting financial barriers, contributing significantly to the successful completion of my research.

I am also profoundly grateful to mentors Dr. Matthew Grace, and Dr. Alicia Magann, who have consistently believed in me and provided unwavering support throughout my quantum information science internship at Sandia National Laboratories through the National Nuclear Security Administration Minority Serving Institutions Internship Program (NNSA- MSIIP).

Finally, to my family, and friends. Your faith in me has been a source of strength and inspiration.

TABLE OF CONTENTS

Abstract	iv
Acknowledgments	vi
List of Tables	xi
List of Figures	xiii
Glossary	xxv
Chapter	
1. Introduction	1
2. Metal-free Matrices for Nanoparticle Synthesis	4
2.1. Porphyrins and Phthalocyanine	4
2.2. Phthalocyanine (Pc)	5
2.2.1. Properties and Applications	5
2.2.2. Role in Nanoparticle Synthesis	6
2.3. Tetraphenylporphyrin (TPP)	7
2.3.1. Properties and Applications	8
2.3.2. Role in Nanoparticle Synthesis	8
2.4. Tetrakis(4-carboxyphenyl)porphyrin (TCPP)	9
2.4.1. Properties and Applications	9
2.4.2. Role in Nanoparticle Synthesis	10
3. Metal-Porphyrins and Metal-Phthalocyanine	12

3.0.1.	Iron Phthalocyanine (FePc)	13
3.0.2.	Iron Porphyrin (FeTPP and FeTCPP)	14
3.0.3.	Size-Dependent Properties	14
3.0.4.	Crystallinity, Amorphism and Nanoparticle Size . . .	15
3.0.5.	Porosity	19
3.0.6.	Magnetic Properties	20
4.	Algorithm	22
4.0.1.	Algorithm Flow	26
4.0.2.	Fourier Transform Filtering	27
4.0.3.	Skeletonization and Node Isolation	28
4.0.4.	Junction Detection	28
4.0.5.	Crystal Structure Identification	28
4.0.6.	Junction Categorization	28
4.0.7.	Porosity Analysis	29
4.0.8.	Visualization	29
5.	Methodology	31
5.1.	Methodology	31
6.	Results	40
6.1.	Magnetic Properties from PPMS Data	41
6.1.1.	Noise Treatment for TPP, TCPP, and Pc Matrices .	42
6.1.2.	Software Approach to Managing Measurement Noise	42

6.1.3.	Influence of Graphene Planes Orientation and Dia-	
	magnetism on Noise	45
6.2.	PXRD Analyses	78
6.2.1.	Size Characterization	88
6.2.2.	Crystallinity and Amorphous Regions	89
6.3.	SEM and EDS Results	89
6.4.	TEM & Algorithm Results	99
7.	Discussion	105
Appendices		
A.	Nanoparticle Analyzer	113
A.1.	Libraries	113
A.2.	Structure Finding Part	113
A.3.	Feature Enhancement Part	116

LIST OF TABLES

Table

4.1. Description of Image Processing Algorithm	30
6.1. Magnetic Properties of Pc Samples Processed Under Different Conditions	48
6.2. Magnetic Properties of TPP Samples under Various Conditions . . .	53
6.3. Magnetic Properties of TCPP Samples under Various Conditions . .	60
6.4. Magnetic Properties of TCPP:TPP Blended Samples under Various Conditions	65
6.5. Magnetic Properties of FePc Samples under Various Conditions . . .	71
6.6. Magnetic Properties of FeTPP Samples under Various Conditions . .	73
6.7. Magnetic Properties of FeTCPP Samples under Various Conditions .	77
6.8. Average nanoparticle sizes with pyrolysis at 900C	88
6.9. Crystallinity and Amorphous Regions with pyrolysis at 900C	89
6.10. Elemental composition of the TCPP matrix with Pyrolysis at 900C- 10min	92
6.11. Elemental composition of the TPP matrix with Pyrolysis at 900C-10min	92
6.12. Elemental composition of the Pc matrix with Pyrolysis at 900C-10min	93
6.13. Elemental composition of the 50% TCPP with 50% TPP matrix with Pyrolysis at 900C-10min	94

6.14. Elemental composition of the 25% TCPP with 75% TPP matrix with Pyrolysis at 900C-10min	95
6.15. Elemental composition of the 75% TCPP with 25% TPP matrix with Pyrolysis at 900C-10min	95
6.16. Elemental composition of the FePc 900C-60min	97
6.17. Elemental composition of the FeTPP 900C-60min	98
6.18. Elemental composition of the FeTCPP 900C-60min	98

LIST OF FIGURES

Figure

- 2.1. Structure of Phthalocyanine (Pc). This diagram shows the molecular structure of Phthalocyanine, a macrocyclic compound containing four isoindole subunits symmetrically arranged around a central nitrogen atom. The molecule is notable for its electronic properties and is widely used in dye production, photodynamic therapy, and as an organic semiconductor. Each hexagon represents a benzene ring, a fundamental component in aromatic compounds, linked to nitrogen atoms that coordinate to a central metal ion in metallophthalocyanines. 5

2.2. Structure of Tetraphenylporphyrin (TPP). This figure illustrates the chemical structure of TPP, which is a synthetic porphyrin with extensive applications in materials science and medicinal chemistry. The core macrocycle, composed of four pyrrole subunits linked via methine bridges (depicted as the nitrogen-containing inner ring), coordinates with various metal ions to form metalloporphyrins. These complexes are crucial for studying catalytic, electronic, and optical properties. The phenyl groups attached at the meso-positions enhance solubility and modify electronic properties, making TPP a valuable compound in the development of photodynamic therapy agents and organic semiconductors.	7
2.3. Structure of Tetrakis(4-carboxyphenyl)porphyrin (TCPP). This diagram illustrates the chemical structure of TCPP, a type of synthetic porphyrin with four carboxyphenyl groups attached at the meso-positions of the porphyrin core. Each carboxyphenyl substituent enhances the solubility of the molecule in polar solvents, which is critical for its applications in catalysis and as a photosensitizer in photodynamic therapy. The porphyrin core, containing nitrogen atoms, can complex with a variety of metal ions, significantly altering the compound's chemical behavior and optical properties.	9

3.1.	Figure shows FeTPP molecule on the left [Inamura et al., 2019], FeTCPP on the center, and FePc on the right [Chilukuri et al., 2020].	12
3.2.	Magnetic field versus normalized moment for samples measured using PPMS. This figure illustrates a typical magnetic hysteresis loop, showing key features such as coercivity, retentivity, and saturation. The loop demonstrates the behavior of magnetic materials when subjected to a varying magnetic field. Source: Iowa State University	20
4.1.	The left represents the state of the art algorithm for carbon. [Sharma et al., 1999]. On the right is our current algorithm which implements new filters, and techniques.	27
5.1.	Temperature profiles for different samples showing the final temperature and duration of treatment.	33
5.2.	Demagnetization sequence, and magnetization for Hysteresis measurement.	36
5.3.	Laboratory pictures from left to right: PPMS, scale, sealing machinery, torch, furnace.	39
6.1.	All hysteresis loops for samples with pyrolysis at 900C for 10 minutes, measuring magnetic moment at 300K with a maximum applied field of $H = 20\text{kOe}$. Inset shows the ferromagnetic region of the loops. Source: Vicente Pena Perez	47

6.2.	All hysteresis loops for samples with pyrolysis at 900C for 10 minutes, measuring magnetic moment at 10K with a maximum applied field of $H = 20\text{kOe}$. Inset shows the ferromagnetic region of the loops. Source: Vicente Pena Perez	48
6.3.	All hysteresis loops for samples with pyrolysis at 900C for 10 minutes, measuring magnetic moment at 300K with a maximum applied field of $H = 20\text{kOe}$. Inset shows the ferromagnetic region of the loops. Source: Vicente Pena Perez	50
6.4.	All hysteresis loops for samples with pyrolysis at 900C for 10 minutes, measuring magnetic moment at 10K with a maximum applied field of $H = 20\text{kOe}$. Inset shows the ferromagnetic region of the loops. Source: Vicente Pena Perez	51
6.5.	All hysteresis loops for samples with pyrolysis at 900C for 10 minutes and oxygen annealed at 150C for 180 minutes, measuring magnetic moment in the range 5K to 300K with a maximum applied field of $H = 20\text{kOe}$. Inset shows the ferromagnetic region of the loops. Source: Vicente Pena Perez	52
6.6.	Hysteresis loops for two samples with pyrolysis at 900C for 10 minutes, measuring magnetic moment at 300K with a maximum applied field of $H = 20\text{kOe}$. Inset shows the ferromagnetic region of the loops. Source: Vicente Pena Perez	55

6.7.	All hysteresis loops for samples with pyrolysis at 900C for 10 minutes, measuring magnetic moment at 300K with a maximum applied field of $H = 20\text{kOe}$. Annealing conditions for all were at 150C for 180 minutes. Inset shows the ferromagnetic region of the loops. Source: Vicente Pena Perez	56
6.8.	Hysteresis loops for two samples with pyrolysis at 900C for 10 minutes, measuring magnetic moment at 10K with a maximum applied field of $H = 20\text{kOe}$. Inset shows the ferromagnetic region of the loops. Source: Vicente Pena Perez	57
6.9.	All hysteresis loops for samples with pyrolysis at 900C for 10 minutes, measuring magnetic moment at 10K with a maximum applied field of $H = 20\text{kOe}$. Annealing conditions for all were at 150C for 180 minutes. Inset shows the ferromagnetic region of the loops. Source: Vicente Pena Perez	58
6.10.	All hysteresis loops for samples with pyrolysis at 900C for 10 minutes and oxygen annealed at 150C for 180 minutes, measuring magnetic moment in the range 5K to 300K with a maximum applied field of $H = 20\text{kOe}$. Inset shows the ferromagnetic region of the loops. Source: Vicente Pena Perez	59

6.11. Hysteresis loops for different concentration of TCPP and TPP with pyrolysis at 900C for 10 minutes, measuring magnetic moment at 10K with a maximum applied field of $H = 20\text{kOe}$. Inset shows the ferromagnetic region of the loops. Source: Vicente Pena Perez	62
6.12. Hysteresis loops for different concentration of TCPP and TPP with pyrolysis at 900C for 10 minutes, measuring magnetic moment at 300K with a maximum applied field of $H = 20\text{kOe}$. Inset shows the ferromagnetic region of the loops. Source: Vicente Pena Perez	63
6.13. Hysteresis loops for different concentration of TCPP and TPP with pyrolysis at 900C for 10 minutes and oxygen annealed at 150C for 180 minutes, measuring magnetic moment at 10K with a maximum applied field of $H = 20\text{kOe}$. Inset shows the ferromagnetic region of the loops. Source: Vicente Pena Perez	64
6.14. All hysteresis loops for FePc with pyrolysis at 900C for different times, measuring magnetic moment at 300K with a maximum applied field of $H = 20\text{kOe}$. Inset shows the ferromagnetic region of the loops. Source: Vicente Pena Perez	67
6.15. All hysteresis loops for FePc with pyrolysis at 900C for different times, measuring magnetic moment at 10K with a maximum applied field of $H = 20\text{kOe}$. Inset shows the ferromagnetic region of the loops. Source: Vicente Pena Perez	68

6.16. All hysteresis loops for FePc with pyrolysis at 900C for different times, measuring magnetic moment at 10K and 300K with a maximum applied field of $H = 20\text{kOe}$. Inset shows the ferromagnetic region of the loops. Source: Vicente Pena Perez	69
6.17. All hysteresis loops for FePc with pyrolysis at 900C for different times, measuring magnetic moment at 10K and 300K with a maximum applied field of $H = 20\text{kOe}$. Annealing conditions for all were at 150C for 180 minutes. Inset shows the ferromagnetic region of the loops. Source: Vicente Pena Perez	70
6.18. All hysteresis loops for FePc with pyrolysis at 900C for different times, measuring magnetic moment at 10K with a maximum applied field of $H = 20\text{kOe}$. Annealing conditions for all were at 150C for 180 minutes. Inset shows the ferromagnetic region of the loops. Source: Vicente Pena Perez	71
6.19. All hysteresis loops with pyrolysis at 900C for 60 minutes, measuring magnetic moment at 10K and 300K with a maximum applied field of $H = 20\text{kOe}$. Inset shows the ferromagnetic region of the loops. Source: Vicente Pena Perez	73

6.20. All hysteresis loops with pyrolysis at 900C for 60 minutes, measuring magnetic moment at 10K and 300K with a maximum applied field of $H = 20\text{kOe}$. Inset shows the ferromagnetic region of the loops. Source: Vicente Pena Perez	75
6.21. All hysteresis loops with pyrolysis at 900C for 60 minutes, measuring magnetic moment at 10K with a maximum applied field of $H = 20\text{kOe}$. Nitrogen and Oxygen annealing are shown with identical conditions 150C for 180 minutes. Inset shows the ferromagnetic region of the loops. Source: Vicente Pena Perez	76
6.22. All hysteresis loops with pyrolysis at 900C for 60 and 180 minutes, measuring magnetic moment at 10K with a maximum applied field of $H = 20\text{kOe}$. Inset shows the ferromagnetic region of the loops. Source: Vicente Pena Perez	77
6.23. PXRD measurements for all carbon matrices: Pc, TCPP, and TPP. They where pyrolyzed at 900C for 10min. Source: Vicente Pena Perez	79
6.24. PXRD measurements for TCPP matrices. They where pyrolyzed at 900C for 10min. Also, annealed plots are shown. Source: Vicente Pena Perez	80
6.25. PXRD measurements for FePc nanoparticles. They where pyrolyzed at 900C at different times. Source: Vicente Pena Perez	83

6.26. PXRD measurements for FeTCPP nanoparticles. They were pyrolyzed at 900C at different times. Source: Vicente Pena Perez	84
6.27. PXRD measurements for FeTCPP nanoparticles. They were pyrolyzed at 900C at different times. Also, annealed plots are shown. Source: Vicente Pena Perez	85
6.28. PXRD measurements for FeTPP nanoparticles. They were pyrolyzed at 900C for 180 minutes. Source: Vicente Pena Perez	86
6.29. PXRD measurements for all nanoparticles. They were pyrolyzed at 900C for 180 minutes. Source: Vicente Pena Perez	87
6.30. SEM images for the carbon matrices: TCPP is shown at a magnification of 10,803 times its size, with an accelerating voltage of 30kV, and scale bar of 10 micrometers. TPP is shown at a magnification of 10,226 times its size, with an accelerating voltage of 30kV, and scale bar of 10 micrometers. Pc is shown at a magnification of 11,683 times its size, with an accelerating voltage of 30kV, and scale bar of 5 micrometers. Source: Vicente Pena Perez	92

6.31. SEM images for the mixed carbon matrices: The first is shown at a magnification of 87,083 times its size, with a accelerating voltage of 10kV, and scale bar of 1 micrometers. Second is shown at a magnification of 13,723 times its size, with a accelerating voltage of 10kV, and scale bar of 5 micrometers. Third is shown at a magnification of 43,289 times its size, with a accelerating voltage of 10kV, and scale bar of 2 micrometers. Source: Vicente Pena Perez	94
6.32. SEM images for FePc: The first is shown at a magnification of 13,855 times its size, with a accelerating voltage of 30kV, and scale bar of 5 micrometers. It shows an overall region of interest for EDS. Second is shown at a magnification of 46,033 times its size, with a accelerating voltage of 30kV, and scale bar of 2 micrometers. This image shows a micro-sphere. Source: Vicente Pena Perez	97
6.33. SEM images for FeTCCP and FeTPP: The first is shown at a magnification of 4,244 times its size, with a accelerating voltage of 30kV, and scale bar of 20 micrometers. Second is shown at a magnification of 4,570 times its size, with a accelerating voltage of 30kV, and scale bar of 20 micrometers. Source: Vicente Pena Perez	98

6.34. Going from left to right: HRSTEM image showing the morphology of the sample at 20nm scale, graphical representation of junction types and counts derived from the algorithm, and skeletonized image of the sample highlighting the detected junctions.	100
6.35. Size characterization of FePc samples with histograms of area, eccentricity, perimeter, and major axis length. For the first field of view, the areas range from 50 to 150 nm^2 , and the length of the major axes from 20 to 75 nm. For the second field of view, we get areas from 5 to 35 nm^2 and length of major axes from 20 to 75nm. Source of first HRSTEM image: Penn State	100
6.36. Labeled regions of FePc samples indicating the size and shape of nanostructures. The first image on the left is the original 50nm range field of view. The second image is the detected nanostructures by the algorithm. Third image is the shape detected over the original image with yellow denoting the perimeter, red the major axes, and blue the minor axes.	101
6.37. Porosity characterization of FePc samples with individual pore measurements. Note that the degree of porosity detected by the algorithm is high, meaning that there is mostly material, and less empty space.	102

- 6.38. Comparative size characterization for FePr samples with histograms of area, eccentricity, perimeter, and major axis length. For the first field of view, the areas range from 0.5 to 2.5 nm^2 , and the length of the major axes from 10 to 50 nm. For the second field of view, we get areas from 100 to 2500 nm^2 and length of major axes from 10 to 250nm. 103
- 6.39. Labeled regions of FePr samples showcasing the distribution of nanostructures, as well as porosity. The first image on the left is the original with the detected nanostructure in color. The second image is the shape detected over the original image with yellow denoting the perimeter, red the major axes, and blue the minor axes. The third image is the porosity. 104

GLOSSARY

Algorithm A process or set of rules to be followed in calculations or other problem-solving operations, especially by a computer.

Avrami-Erofeev Model A mathematical model that describes the kinetics of phase change processes.

BET Theory A theory that explains the physical adsorption of gas molecules on a solid surface and serves as the basis for an important analysis technique for the measurement of the specific surface area of materials.

BJH Method Barret-Joyner-Halenda method; an extension of the BET theory that analyzes the pore size distribution of a material.

Crystallinity The degree to which a solid material has a crystal structure, consisting of a repetitive and orderly arrangement of atoms.

Deagglomeration The process of breaking down aggregates into finer particles.

FePc Iron Phthalocyanine; a macrocyclic compound with a central iron atom.

FePr Iron Porphyrin; a heme-like compound with a central iron atom.

Fourier Transform A mathematical transform that decomposes a function (often a function of time, or a signal) into its constituent frequencies.

HRTEM High-Resolution Transmission Electron Microscopy; a microscopy technique that allows imaging at atomic scales.

Junctions Points in a network or structure where multiple paths meet or cross.

Kissinger Model A model used to describe the thermal activation of a chemical reaction rate by an Arrhenius equation.

Langmuir Surface Area Analysis A method to determine the monolayer adsorption capacity of a material.

Micropore Area and Volume Analysis Techniques to characterize the surface area and volume of micropores within materials.

Nanoparticle A microscopic particle with at least one dimension less than 100 nm.

Otsu's Thresholding A method used in image processing to automatically perform clustering-based image thresholding.

Porosity The measure of the void spaces in a material, and is a fraction of the volume of voids over the total volume.

PPMS Physical Property Measurement System; an instrument used to measure the physical properties of materials.

PXRD Powder X-ray Diffraction; a technique used to characterize the crystallographic structure, crystalline phases, and other structural parameters of materials.

SEM Scanning Electron Microscope; a type of electron microscope that produces images of a sample by scanning it with a focused beam of electrons.

Skeletonization The process of reducing a shape into a skeletal form, important in the analysis of complex structures.

CHAPTER 1

Introduction

This thesis presents a comprehensive approach to magnetic nanostructure characterization, integrating advanced methodologies from multiple research studies. Our work is not just an exploration of magnetic nanostructures but the work of interdisciplinary research, bringing together various technological, mathematical, and physical ideas to better understand the magnetic and structural properties of nanoparticles.

Magnetic and electronic properties of nanoparticles have long been on the observance of the scientific community not only from texture analysis and lattice fringe imaging but also from the micro and nano structural analysis as those shown in analysis of Coal char using High-Resolution Transmission Electron Microscopy (HRTEM), as demonstrated by Sharma, Kyotani, and Tomita. [Sharma et al., 1999]

With the ongoing technological development of programming techniques, and technologies, it only makes sense to move along with the wave of new cutting-edge algorithms that will facilitate the analysis of such nanoparticle properties. [Le Pouliquen et al., 2005] Our focus is on Porphyrin (Pr) and Phthalocyanine (Pc) nanoparticles. However, we try to work on previous technological achievements as described in “A new quantitative approach for microstructural analysis of coal char using HRTEM images,” [Sharma et al., 1999]. Here, we employ fil-

tration techniques and computer algorithms on Scanning Electron Microscope (SEM) images by mapping them to analyze magnetic nanostructures at the atomic level on the Powder X-ray diffraction PXRD. This approach allows us to comprehensively characterize nanostructures in both Pc and Pr nanoparticles, capturing layer sizes, interlayer spacing, distribution of the layers per stack, in general, its morphology, and from there, we construct a mapping to the elemental composition of the nanoparticle itself. We are able to map from the SEM image to the PXRD elemental analysis, advancing the analysis to be complete pixel by pixel.

Our methodology also incorporates a two-step image extraction process similar to Sharma et al.'s work. [Sharma et al., 1999] We employ noise reduction using sophisticated filters such as Gaussian blur, contrast stretching to enhance the dynamic range, adaptive histogram equalization to improve local contrast, applying morphological closing to connect regions and smooth particles, edge enhancement via Sobel filtering, and Unsharp mask to sharpen the image followed by the mathematical separation and reconnection of layers, ensuring that our analysis retains both accuracy and detail. [Pré et al., 2013] This approach aligns with the innovative filtration and processing techniques developed by Sharma et al., which greatly enhance the reliability and precision of structural analysis in HRTEM images.

Furthermore, like that of Sharma, Kyotani, and Tomita, our work aims to eliminate human subjectivity from the image analysis process. By employing a computer algorithm for image analysis, we ensure that our results are precise but also

reproducible and generalizable across various nanostructured materials.

CHAPTER 2

Metal-free Matrices for Nanoparticle Synthesis

2.1 Porphyrins and Phthalocyanine

The synthesis of metal nanoparticles requires a solid understanding of the metal-free matrices that serve as the foundational precursors. These matrices not only dictate the fundamental structure but also influence the resultant properties of the synthesized nanoparticles. This chapter provides an overview of three critical precursors: Phthalocyanine (Pc), Tetraphenylporphyrin (TPP), and Tetrakis(4-carboxyphenyl)porphyrin (TCPP), each with unique characteristics that make them ideal for metal nanoparticle synthesis. The main focus of this chapter is to set the foundation for the three matrices precursors.

2.2 Phthalocyanine (Pc)

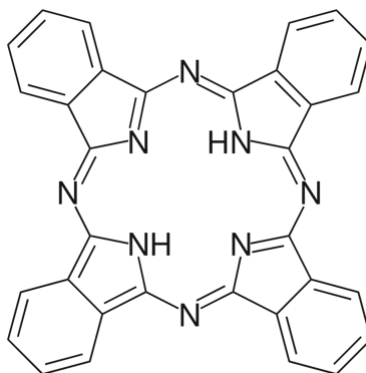


Figure 2.1: Structure of Phthalocyanine (Pc). This diagram shows the molecular structure of Phthalocyanine, a macrocyclic compound containing four isoindole subunits symmetrically arranged around a central nitrogen atom. The molecule is notable for its electronic properties and is widely used in dye production, photodynamic therapy, and as an organic semiconductor. Each hexagon represents a benzene ring, a fundamental component in aromatic compounds, linked to nitrogen atoms that coordinate to a central metal ion in metallophthalocyanines.

2.2.1 Properties and Applications

Phthalocyanine ($C_{32}H_{18}N_8$) is a macrocyclic compound with remarkable electronic and optical properties due to its extensive π -conjugation. It is widely used in dyeing, organic semiconductors, and photovoltaic devices because of its stable chemical properties and intense blue or green color.

2.2.2 Role in Nanoparticle Synthesis

In nanoparticle synthesis, Pc serves as a stable matrix that can facilitate the control of the size and distribution of the metal nanoparticles. The π -conjugation also allows for efficient electron transfer, influencing the electronic properties of the nanoparticles.

2.3 Tetraphenylporphyrin (TPP)

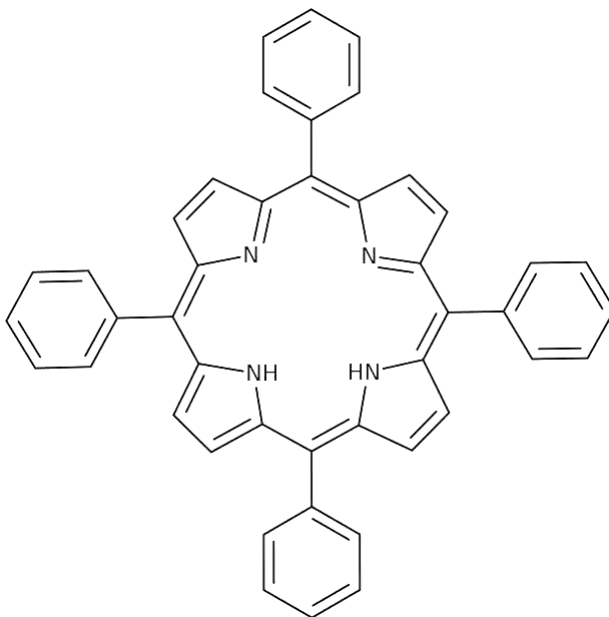


Figure 2.2: Structure of Tetraphenylporphyrin (TPP). This figure illustrates the chemical structure of TPP, which is a synthetic porphyrin with extensive applications in materials science and medicinal chemistry. The core macrocycle, composed of four pyrrole subunits linked via methine bridges (depicted as the nitrogen-containing inner ring), coordinates with various metal ions to form metalloporphyrins. These complexes are crucial for studying catalytic, electronic, and optical properties. The phenyl groups attached at the meso-positions enhance solubility and modify electronic properties, making TPP a valuable compound in the development of photodynamic therapy agents and organic semiconductors.

2.3.1 Properties and Applications

Tetraphenylporphyrin ($C_{44}H_{30}N_4$) closely resembles the natural porphyrins and is crucial in the study of biomimetic systems. It models the active sites of metalloproteins and is pivotal in research related to photodynamic therapy and solar energy conversion.

2.3.2 Role in Nanoparticle Synthesis

The synthetic flexibility of TPP allows for the introduction of various functional groups, which can enhance the affinity for metal ions, thus controlling the formation and stabilization of the metal nanoparticles.

2.4 Tetrakis(4-carboxyphenyl)porphyrin (TCPP)

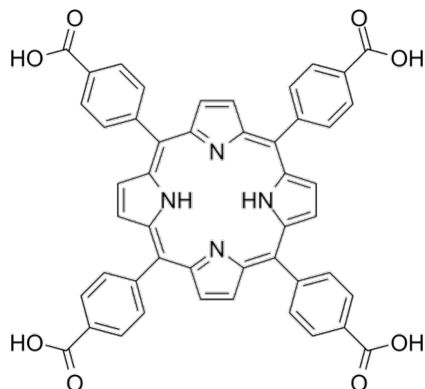


Figure 2.3: Structure of Tetrakis(4-carboxyphenyl)porphyrin (TCPP). This diagram illustrates the chemical structure of TCPP, a type of synthetic porphyrin with four carboxyphenyl groups attached at the meso-positions of the porphyrin core. Each carboxyphenyl substituent enhances the solubility of the molecule in polar solvents, which is critical for its applications in catalysis and as a photosensitizer in photodynamic therapy. The porphyrin core, containing nitrogen atoms, can complex with a variety of metal ions, significantly altering the compound's chemical behavior and optical properties.

2.4.1 Properties and Applications

TCPP ($C_{48}H_{30}N_4O_8$) is a porphyrin derivative with enhanced solubility and reactivity due to the presence of carboxyphenyl groups. Its applications range from catalysis to sensor development and photodynamic therapy.

2.4.2 Role in Nanoparticle Synthesis

The carboxylic groups in TCPP not only provide solubility but also offer sites for subsequent functionalization, thereby influencing the nanoparticle surface chemistry and introducing new properties to the metallic centers.

The choice of the metal-free matrix is a critical step in the synthesis of metal nanoparticles. The properties of Pc, TPP, and TCPP, such as their π -conjugation systems and functional groups, provide a versatile platform for tailoring the characteristics of metal nanoparticles.

Distinct variations in magnetic properties emerge from the complexation of metal ions with Phthalocyanine (Pc), Tetraphenylporphyrin (TPP), and Tetrakis(4-carboxyphenyl)porphyrin (TCPP), primarily influenced by the structural characteristics and electronic environments of each macrocycle.[Inamura et al., 2019]. Pc, with its symmetric, nitrogen-rich core, tends to form highly stable and evenly distributed complexes with metals such as Cu and Fe, which can exhibit paramagnetic properties depending on the oxidation state and coordination geometry of the metal ion. In contrast, TPP, with its larger, more flexible structure due to the phenyl substituents at the meso positions, can accommodate a variety of metal ions, potentially leading to diverse magnetic behaviors including diamagnetism in its free state and varying degrees of paramagnetism when complexed with metals like Mn or Co. TCPP stands out due to its additional carboxyphenyl groups, which not only enhance solubility and subsequent interaction with metal ions but also facilitate the attachment

of multiple metal centers. This can lead to intricate magnetic interactions such as antiferromagnetic or ferromagnetic coupling between adjacent metal ions, contingent upon the method of nanoparticle synthesis and the spatial arrangement of the TCPP ligands around the metal centers. Thus, the choice of metal-free matrix and its specific interaction with metal ions crucially dictates the magnetic characteristics of the synthesized nanoparticles, offering tailored functionalities for advanced material applications. [Chilukuri et al., 2020]

These matrices open avenues for the development of advanced materials with applications in electronics, catalysis, and quantum technologies.

CHAPTER 3

Metal-Porphyrins and Metal-Phthalocyanine

Before diving into the heart of our algorithm, we have to define the basis of our work.

First, by defining what a metal Pr and Pc precursor molecule looks like.

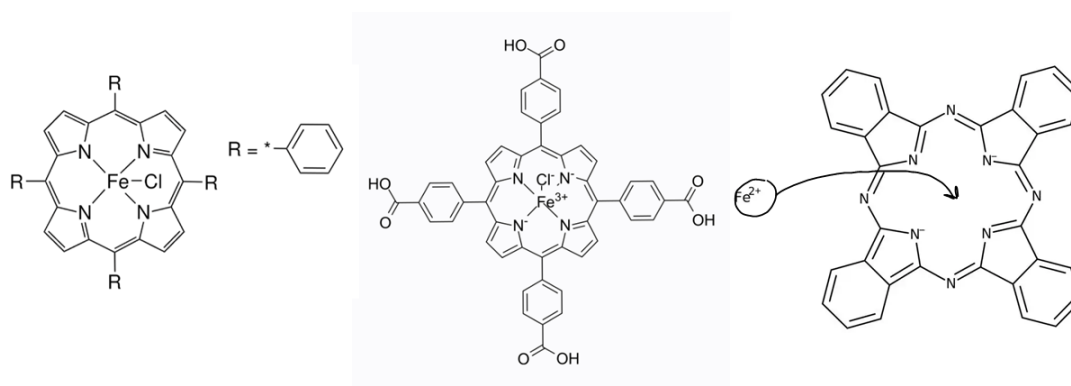


Figure 3.1: Figure shows FeTPP molecule on the left [Inamura et al., 2019], FeTCPP on the center, and FePc on the right [Chilukuri et al., 2020].

Note that in both molecules, the central element is a metal. We selected iron (Fe), and pure Pc as well as Pr. The structure of Pc includes an inner nitrogen (N) shell, and outer carbon (C) one. The Pc structure is characterized by an aromatic macrocycle, which is composed of four isoindole units connected by nitro-

gen atoms, which form a planar, ring-like structure. [Inamura et al., 2019] Nonetheless, the Pr structure is also a macrocyclic ring, but with a slightly variation, they consist of four pyrrole subunits interconnected via methine bridges (=CH– groups) [Chilukuri et al., 2020].

Both structures are used in many applications such as dyes and pigments, as well as catalysts in chemical reactions. Both molecules can bind metal ions at the center which can modify their electronic and chemical properties.

3.0.1 Iron Phthalocyanine (FePc)

When iron is the central metal in a phthalocyanine complex, it imparts magnetic properties to the molecule due to its unpaired electrons. FePc is known for its catalytic properties, including in electrocatalysis and photocatalysis. [Neamtu et al., 2020]. It is also used in gas sensors and as a semiconductor material. The specific properties of FePc include a high degree of thermal stability and a unique electronic absorption spectrum due to the d-d transitions of the iron ion. [Stephenson and Bell, 2007]

Nanoparticle

Studies indicate that FePc nanoparticles exhibit enhanced oxygen reduction reaction (ORR) performance when there's axial coordination with oxygen, due to induced electronic localization. This characteristic could potentially boost the performance of FePc as a non-precious catalyst in fuel cells. Advanced characterization techniques like X-ray diffraction (XRD) reveal insights into the coordination environment and electronic structure changes in these nanoparticles, critical for their catalytic function

[Chen et al., 2020]

3.0.2 Iron Porphyrin (FeTPP and FeTCPP)

Iron porphyrins are biologically significant since they are analogs of heme, the active site in hemoglobin and myoglobin. Iron in porphyrin has different oxidation states, which can bind to oxygen or other ligands. This ability to coordinate to other molecules makes iron porphyrins important in studying oxygen transport and electron transfer processes. In the context of material science, Fe-Pr complexes have been investigated for their use in catalysis, such as in the oxidation of hydrocarbons, and in the development of organic electronic devices.[Nelson et al.,]

Nanoparticle

FePr nanoparticles annealed by oxygen and nitrogen can significantly influence their magnetic properties. Structural and magnetic characterizations of these nanoparticles have been performed using similar techniques to those used for FePc nanoparticles, such as XRD, XPS, and high-resolution SEM/STEM images. These characterizations revealed the potential of these materials for applications in magnetic hyperthermia medical treatments, a technique used for cancer therapy. [Kocharian et al.,]

3.0.3 Size-Dependent Properties

SEM and HRTEM have been useful techniques to analyze a wide range of micro and nano-structures, and help understanding their sizes in correlation to their method of synthesizing. Such studies had been conducting in coal char at an atomic level.

[Sharma et al., 1999]. By properly analyzing the structure quantitatively, a filtration technique can be implemented. Furthermore, we proposed that there must be a size dependence on time and temperature of pyrolysis. The experimental results will show this conjecture.

3.0.4 Crystallinity, Amorphism and Nanoparticle Size

Since crystallinity and amorphism are the most important categories when it comes to nano-structures, it is necessary to review their definitions. Crystalline materials are characterized by a well-ordered atomic structure with a repeating pattern, whereas amorphous materials lack this long-range order. Powder X-Ray Diffraction (PXRD or XRD) is a technique used in combination to SEM/TEM to determine the degree of crystallinity or their lack of arrangement, such material could potentially be amorphous.

The so called Bragg's Law is fundamental to understanding XRD patterns.

$$n\lambda = 2d \sin \theta \tag{3.1}$$

where:

- n is the order of the diffraction, typically 1 for first-order diffractions.
- λ is the wavelength of the incident X-ray beam.
- d is the distance between the crystal planes that contribute to diffraction.
- θ is the angle of incidence at which X-rays are diffracted.

Cubic Crystal Structures

For cubic systems, the lattice constant a and the Miller indices (h, k, l) fully describe the spacing between planes via simple geometric principles.

Derivation for Cubic Structures

Consider a cube with side a . The distance between two parallel planes described by Miller indices (h, k, l) can be derived from the geometry of the cube.

1. **Vector Representation:** A plane in a cubic crystal can be represented by its normal vector $\vec{n} = (h, k, l)$.

2. **Point on the Plane:** A point (x, y, z) lies on the plane if it satisfies the equation $hx + ky + lz = d$, where d is a constant.

3. **Intercept Form:** If this plane cuts the axes at $a/h, a/k$, and a/l , then the plane equation can be rewritten in intercept form as:

$$\frac{x}{a/h} + \frac{y}{a/k} + \frac{z}{a/l} = 1 \quad (3.2)$$

4. **Perpendicular Distance:** The distance from the origin to the plane (which is d), is the length of the projection of any vector from the origin onto the normal vector of the plane. This projection, using the dot product and normalizing by the magnitude of \vec{n} , gives:

$$d = \frac{|\vec{r} \cdot \vec{n}|}{|\vec{n}|} \quad (3.3)$$

where $\vec{r} = (x, y, z)$ and $|\vec{n}| = \sqrt{h^2 + k^2 + l^2}$.

5. **General Formula:** The distance d for any cubic system with Miller indices

(h, k, l) thus becomes:

$$d_{hkl} = \frac{a}{\sqrt{h^2 + k^2 + l^2}} \quad (3.4)$$

Hexagonal Crystal Structures

Hexagonal structures have two lattice constants a and c , reflecting different spacings in the basal plane and along the c -axis.

Derivation for Hexagonal Structures

The derivation for the d -spacing in hexagonal crystals involves considering the unique geometry of the lattice:

1. **Geometry of the Basal Plane:** The basal plane has Miller indices $(h, k, 0)$ with the third axis, i , being implicit in hexagonal indexing.
2. **Distance Calculation:** The vertical distance (along c) and horizontal distances in the basal plane are combined using Pythagoras' theorem:

$$d_{hkl} = \frac{a}{\sqrt{\frac{4}{3}(h^2 + hk + k^2) + \frac{l^2 a^2}{c^2}}} \quad (3.5)$$

Nanoparticle Size Calculation

The Scherrer Equation is utilized to estimate the size of crystalline nanoparticles from XRD data. This equation relates the broadening of the diffraction peaks in the XRD pattern, primarily due to the small size of the particles, to their average crystallite size. The equation is given by:

$$L = \frac{K\lambda}{\beta \cos \theta} \quad (3.6)$$

where L is the mean size of the crystalline domains (often called the crystallite size), K is the shape factor (with a typical value of about 0.9), λ is the X-ray wavelength, β is the full-width at half-maximum (FWHM) of the peak in radians, and θ is the Bragg angle.

Crystallinity Calculation

Crystallinity is calculated as the ratio of the crystalline area under the XRD peaks to the total area under the XRD curve. This value is expressed as a percentage and provides a measure of the proportion of crystalline material in the sample. The areas are calculated using numerical integration, and where peaks overlap, a merging algorithm adjusts the estimation to avoid overcounting. The adjusted crystallinity calculation method is described as:

$$\text{Crystallinity} = \left(\frac{\sum \text{Merged Peak Areas}}{\text{Total Area}} \right) \times 100\% \quad (3.7)$$

where the merged peak areas are averaged to mitigate the effects of overlapping peaks.

Graphitization Calculation

Graphitization is assessed by analyzing the relative intensities of graphite-specific peaks in the XRD pattern. The degree of graphitization is calculated using the intensity of the graphite peaks relative to the total intensity of all peaks observed:

$$\text{Graphitization} = \left(\frac{\text{Sum of Graphite Peak Intensities}}{\text{Total Peak Intensities}} \right) \times 100\% \quad (3.8)$$

This quantification provides an indication of the extent to which carbon in the sample has converted into its crystalline graphite form.

Peak Merging Technique

To address the issue of overlapping peaks in the crystallinity calculation, a peak merging technique is employed. Peaks that are within a certain threshold angular distance from each other are considered for merging. The merged peak area is calculated as the average of the areas of the overlapping peaks, providing a more accurate representation of the crystalline material in the sample. This method ensures that the crystallinity is not overestimated due to peak overlap.

3.0.5 Porosity

Porosity refers to the presence of pores or voids within the structure of a nanoparticle. These voids can represent great part of the nanostructure's mechanical, thermal, and chemical properties. They can be classified as open, closed, and total porosity or voids.[Barrett et al., 1951]

3.0.6 Magnetic Properties

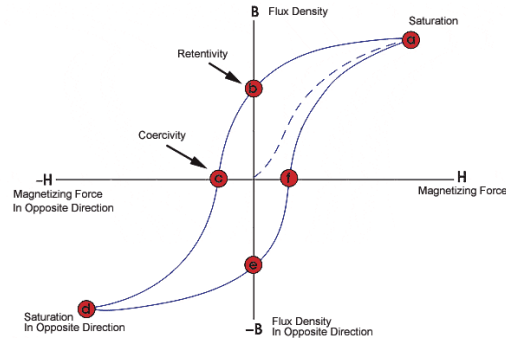


Figure 3.2: Magnetic field versus normalized moment for samples measured using PPMS. This figure illustrates a typical magnetic hysteresis loop, showing key features such as coercivity, retentivity, and saturation. The loop demonstrates the behavior of magnetic materials when subjected to a varying magnetic field. Source: Iowa State University

- **Saturation (A & D):** Points where increasing the magnetizing force no longer increases the magnetization, indicating that all magnetic domains are aligned.
- **Retentivity (B):** The residual magnetism or magnetic flux density remaining in the material after the magnetizing force is removed, indicative of the material's ability to retain magnetization.
- **Coercivity (C):** The required reverse magnetic field strength to bring the magnetization to zero, a measure of the material's resistance to becoming demagnetized.

The dashed line in Figure 3.2 represents the initial magnetization curve, and the

solid line shows the behavior after the material has reached its initial saturation, highlighting the material's magnetic hysteresis.

Measuring Porosity

The BET theory is fundamental for determining the specific surface area of materials. It is based on the adsorption of gas molecules on the material surface and is described by the equation:

$$\frac{1}{V(1 - P/P_0)} = \frac{C - 1}{V_m C P_0} \left(\frac{P}{P_0} \right) + \frac{1}{V_m C} \quad (3.9)$$

where V is the volume of gas adsorbed, P_0 and P are saturation and equilibrium pressures, V_m is the monolayer adsorbed gas quantity, and C is the BET constant. [Barrett et al., 1951]

CHAPTER 4

Algorithm

The script is designed for processing High-Resolution Transmission Electron Microscopy (HRTEM) images. It encompasses various stages of image processing, including filtering, skeletonization, fringe reconnection, and junction categorization. Key libraries utilized include NumPy for numerical operations, SciPy for scientific computations, and scikit-image for image processing tasks. Refer to the Appendix A to see detailed functions of the algorithm.

- **Fourier Transforms:** The Fourier transform is essential for converting an image from the spatial domain to the frequency domain. The two-dimensional Fourier transform of an image $f(x, y)$ is given by:

$$F(u, v) = \int_{-\infty}^{\infty} \int_{-\infty}^{\infty} f(x, y) e^{-i2\pi(ux+vy)} dx dy \quad (4.1)$$

where $F(u, v)$ is the Fourier transform of $f(x, y)$, and u, v are the spatial frequencies.[Joubert et al., 2023]

- **Otsu's Thresholding:** Otsu's thresholding is an image segmentation technique that determines an optimal threshold value T to separate an image into two classes. This method aims to minimize the weighted within-class variance,

represented by the equation

$$\sigma_w^2(T) = q_1(T)\sigma_1^2(T) + q_2(T)\sigma_2^2(T) \quad (4.2)$$

where q_1, q_2 are the probabilities of the two classes separated by T , and σ_1^2, σ_2^2 are variances of these classes. The selected threshold T effectively maximizes the between-class variance, leading to better class separability in the image.

- **Skeletonization:** Skeletonization reduces binary images into a minimal representation, which can be conceptually understood as:

$$S = \bigcap_{i=1}^N (I \ominus k_i) \quad (4.3)$$

where S is the skeleton, I is the original image, \ominus denotes morphological erosion, and k_i are structuring elements applied iteratively.

– Zigzag:

$$\begin{pmatrix} 1 & 0 & 0 & 1 \\ 0 & 1 & 0 & 0 \\ 1 & 0 & 0 & 1 \\ 0 & 1 & 0 & 0 \end{pmatrix}$$

– Armchair:

$$\begin{pmatrix} 0 & 1 & 1 & 0 \\ 1 & 0 & 0 & 1 \\ 0 & 1 & 1 & 0 \\ 1 & 0 & 0 & 1 \end{pmatrix}$$

– X Pattern:

$$\begin{pmatrix} 1 & 0 & 0 & 1 \\ 0 & 1 & 1 & 0 \\ 0 & 1 & 1 & 0 \\ 1 & 0 & 0 & 1 \end{pmatrix}$$

– T Pattern:

$$\begin{pmatrix} 0 & 1 & 1 & 1 \\ 0 & 0 & 1 & 0 \\ 0 & 0 & 1 & 0 \\ 0 & 0 & 0 & 0 \end{pmatrix}$$

– Y Pattern:

$$\begin{pmatrix} 0 & 1 & 0 & 1 \\ 0 & 0 & 1 & 0 \\ 0 & 0 & 1 & 0 \\ 0 & 0 & 1 & 0 \end{pmatrix}$$

– L Pattern:

$$\begin{pmatrix} 1 & 0 & 0 & 0 \\ 1 & 0 & 0 & 0 \\ 1 & 0 & 0 & 0 \\ 1 & 1 & 1 & 0 \end{pmatrix}$$

- **Porosity Calculation:** Total porosity P of an image can be calculated as the ratio of the pore area to the total area:

$$P = \frac{\text{Total Pore Area}}{\text{Total Area}} = \frac{\sum \text{binary_image}}{\text{size of binary_image}} \quad (4.4)$$

- **Examples of Image Processing Techniques**

- (1) **Fourier Transforms:**

Consider an image function $f(x, y)$ defined as a simple checkerboard pattern with alternating black and white squares. The function can be mathematically modeled as:

$$f(x, y) = \text{sign}(\sin(x) \cdot \sin(y))$$

Its Fourier transform $F(u, v)$ is:

$$F(u, v) = \int_{-\infty}^{\infty} \int_{-\infty}^{\infty} \text{sign}(\sin(x) \cdot \sin(y)) e^{-i2\pi(ux+vy)} dx dy$$

This transform will show peaks at frequencies that correspond to the size of the squares in the checkerboard pattern.

(2) **Otsu's Thresholding:**

For an image with a bimodal histogram (e.g., an image with a clear distinction between the background and the foreground), let's assume the pixel intensity values roughly follow two normal distributions centered at around 100px and 200px, respectively. Otsu's method calculates the optimal threshold T by minimizing:

$$\sigma_w^2(T) = \frac{n_1(T)}{N} \sigma_1^2(T) + \frac{n_2(T)}{N} \sigma_2^2(T)$$

where $n_1(T), n_2(T)$ are the number of pixels in each class divided by T , $\sigma_1^2(T), \sigma_2^2(T)$ are their variances, and N is the total number of pixels.

(3) **Skeletonization:**

Consider a binary image of a filled rectangle. The goal of skeletonization is to reduce this rectangle to a line (its skeleton) that represents the middle axis. The process involves iterative morphological erosion until the structure cannot be eroded further:

$$S = \bigcap_{i=1}^N (I \ominus k_i)$$

where I is the original image, \ominus denotes the morphological erosion, and k_i are structuring elements. The result S will be the minimal set of pixels that retain the geometrical and topological properties of the rectangle.

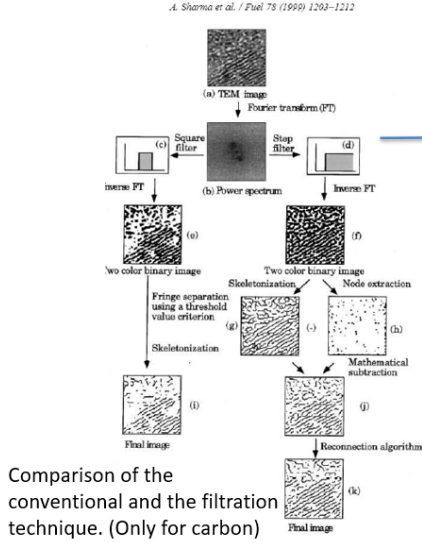
4.0.1 Algorithm Flow

Here we delineate the flow diagram of the algorithm designed for the analysis of SEM, PXRD, and PPMS data. The Python script is executable via the console; however, for the purposes of debugging, Jupyter-lab was the preferred environment.

The fundamental steps of the algorithm are as follows:

- (1) **File Selection:** The user specifies the directory path containing the SEM, PXRD, and PPMS files to be processed.
- (2) **SEM Image Processing:** The algorithm begins by applying the filters previously described to the SEM image to enhance feature visibility.
- (3) **Junction Detection:** Subsequent to image filtering, the algorithm identifies junctions within the image and attempts to reconnect them, thereby refining the image of the layers.
- (4) **Nanostructure Characterization:** Following the enhancement of the image, the algorithm proceeds to detect nanostructures. It categorizes them according to their area and the length of the major axis.
- (5) **Porosity Calculation:** Utilizing the identified areas, the algorithm calculates the porosity of the sample.
- (6) **Data Visualization:** Finally, the algorithm presents the results through histograms and overlays the identified structures onto the original SEM image for a comparative analysis.

Previous work



Current work

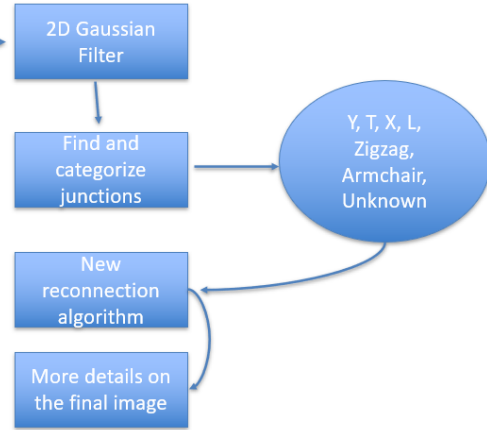


Figure 4.1: The left represents the state of the art algorithm for carbon. [Sharma et al., 1999]. On the right is our current algorithm which implements new filters, and techniques.

4.0.2 Fourier Transform Filtering

The `apply_step_filter` function applies a Fourier transform to the image, filters frequencies using a step function within a specified radius, and applies an inverse Fourier transform. This method is used for noise reduction and to highlight features of interest by removing high-frequency components.

$$F(u, v) = \mathcal{F}\{f(x, y)\} \quad (4.5)$$

$$f_{filtered}(x, y) = \mathcal{F}^{-1}\{F(u, v)H(u, v)\} \quad (4.6)$$

Where $H(u, v)$ is a step function that is 1 within a specified radius and 0 otherwise.

4.0.3 Skeletonization and Node Isolation

The `skeletonize_and_isolate_nodes` function converts the filtered image to a binary format using Otsu's threshold, then applies skeletonization to reduce image structures to their minimal form. Nodes or junctions within the skeleton are further isolated based on their intensity.

4.0.4 Junction Detection

Junctions are detected by labeling the skeletonized image and analyzing connectivity using the region properties. Each labeled segment is examined for junction points where three or more lines meet.

4.0.5 Crystal Structure Identification

Pre-defined templates for different crystal structures (e.g., hematite, magnetite, maghemite) are matched against the image using a pattern matching technique. This allows for the identification of specific nanoparticle types based on their structural patterns.

4.0.6 Junction Categorization

Identified junctions are categorized into types (Y, T, X, L) based on their geometric configuration in the skeleton. This categorization helps in understanding the connectivity and network structure of the particles.

4.0.7 Porosity Analysis

The script can calculate porosity by converting the image to a binary form where pores are marked, and then computing the ratio of pore area to the total area. This analysis is crucial for characterizing our nanoparticles from being completely empty (shell structure), or solid spheres. If the value obtained by the algorithm is closer to one, it means that the object or region analyzed is mostly empty (high porosity), and if it is less than one, then it's less porous. [Potter, Matthew E. Cite]

4.0.8 Visualization

Various visualization functions are included to plot and analyze the results, such as displaying junction types, overlaying labeled regions on the original image, and plotting histograms of particle properties.

Function Name	Description
<code>apply_step_filter(image, radius)</code>	Conducts a Fourier transform on an image, filters it using a step function, and applies an inverse Fourier transform to obtain a filtered image.
<code>skeletonize_and_isolate_nodes(filtered_image, node_threshold_factor)</code>	Skeletonizes the filtered image and isolates nodes by adjusting the threshold, producing both skeleton and nodes-only images.
<code>find_junctions(skeleton)</code>	Identifies junctions in the skeletonized image and categorizes them into types (Y, T, X, L, or unknown), including the functionality for detecting specific crystal structures.
<code>categorize_junctions(junctions, skeleton)</code>	Further categorizes junctions into specific types and identifies crystal structures such as hematite, magnetite, and maghemite.
<code>analyze_and_plot_junctions(categorized_links)</code>	Analyzes junction types and visualizes them in a bar plot, showcasing their distribution.
<code>process_hrtem_image(image_path)</code>	Processes an HRTEM image through filtering, skeletonizing, reconnecting fringes, categorizing junctions, and detecting crystal structures.
<code>process_tem_image_simple(image_path, sigma, size_threshold)</code>	Processes TEM images to identify and label particles using Gaussian filtering and thresholding techniques.
<code>analyze_particle_properties_simple(properties)</code>	Conducts analysis on particles' properties identified in TEM images, generating histograms and statistical insights.
<code>process_tem_image(image_path, pixel_sizes, sigma, size_threshold)</code>	Similar to <code>process_tem_image_simple</code> but adjusts for pixel size to enable nanometer-scale analysis.
<code>analyze_and_visualize_particle_properties(image_path, properties_nm, labeled_image, pixel_size_nm)</code>	Analyzes and visualizes particle properties at the nanometer scale and overlays labeled regions on the original TEM image.
<code>calculate_porosity(binary_image, labeled_image)</code>	Calculates porosity for individual regions and the total image based on binary image analysis.
<code>generate_crystal_template(crystal_type)</code>	Generates templates for various crystal structures (e.g., hematite, magnetite, maghemite) for pattern matching.
<code>pattern_match(skeleton, pattern)</code>	Applies pattern matching to skeletonized images to identify specific crystal structures.

Table 4.1: Description of Image Processing Algorithm

CHAPTER 5

Methodology

5.1 Methodology

The methodology of this research encompasses preparation of the precursor materials FePc, FeTPP and FeTCPP. Measuring their corresponding masses, sealing the samples under vacuum by applying an oxygen + acetylene torch, then on the furnace we set up different temperatures. Additionally, we proceed with the deagglomeration process in which we open the sealed samples, grind them with pestle and mortar, and apply ultrasonic dispersion. Finally, we prepare the samples to measure different characteristics. The following topics are integral to our approach:

(1) **Selecting Precursor**

- We initiate the process by accurately measuring the mass of our precursor. First, we tare the weigh paper on the balance. Then, using a plastic scoop, we add the sample gradually until the desired mass, typically between 100-200 grams, is achieved. This precision is crucial for consistent results in pyrolysis.
- The sample is then transferred into the quartz tube using an innovative method designed to prevent contamination and contact with the tube's inner walls. We shape the weigh paper into a rhomboidal form, attach

it to the end of a plastic rod, and place the sample in this 'taco-shaped' paper. This assembly is carefully inserted into the quartz tube, where the sample is gently deposited by sliding the rod deep into the tube and ensuring the sample is left in the correct position.

(2) **Vacuum/No Vacuum Sealing: Oxygen + Acetylene Flame**

- We prepare the tube by connecting it to a vacuum pump via a hose, which allows us to evacuate the air and achieve an internal pressure of approximately 10^{-4} Torr.
- It is crucial to understand the temperature gradient of the torch flame used for sealing. The outer layer of the flame displays an orange to yellow hue, indicative of cooler temperatures, while the inner core is blue, signifying much higher temperatures ranging from about $1,000^{\circ}\text{C}$ to $3,500^{\circ}\text{C}$.
- We ensure that the effects of the flame on the sample are negligible by maintaining a distance of more than 20 cm from the seal point to the sample. This precaution prevents direct exposure to the heat and thermal gradients of the flame, thereby preserving the sample's structural integrity and morphological properties.

(3) **Pyrolysis**

- Here is where the nanoparticles are formed by altering the structural properties through heat treatment. The temperatures employed range from 250 degrees Celsius to 900 degrees Celsius. The duration of heat application

also varies, as it is a critical factor in determining the size and properties of the nanoparticles synthesized. The time the sample remains in the furnace can significantly influence the kinetics of nanoparticle formation and growth.

- For the results presented, we maintained a constant temperature of 900 degrees Celsius. The duration of the heat treatment varied, with one set of samples being treated for 10 minutes and another set for 60, 120 and 180 minutes. These variations in treatment time allow us to analyze the effects of heat exposure duration on the nanoparticle synthesis process.

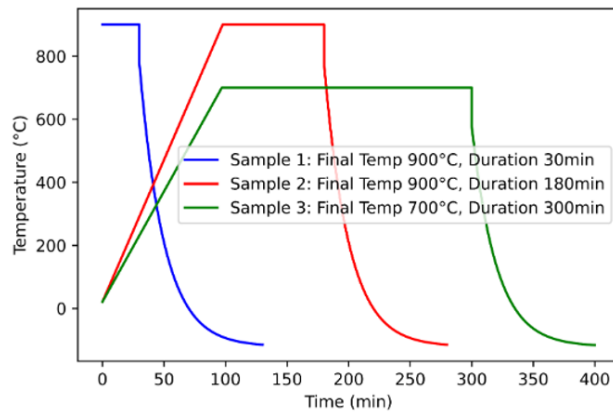


Figure 5.1: Temperature profiles for different samples showing the final temperature and duration of treatment.

(4) Deagglomeration

- Upon completing the pyrolysis, we carefully open the sealed tubes and begin the deagglomeration by manually grinding the sample using a pestle

and mortar. This step is critical for breaking down the sample into finer particles, which facilitates a more detailed analysis of the nanoparticles. We also meticulously remove any glass shards from the cutting of the tube to ensure sample purity.

- The sample then undergoes ultrasonic dispersion in isopropyl alcohol (IPA) for at least 60 minutes, enhancing particle separation.
- Subsequent to drying, the sample is subjected to centrifuge treatment for 10 minutes, allowing particles of different densities to separate in the holder.
- Lastly, the sample is placed in a magnetic separator for 10 minutes, which helps in determining the initial magnetization of the sample. Following this, it is placed in a desiccator under vacuum and left to dry overnight to remove any residual solvent.
- Overall, the deagglomeration process serves as a crucial activation step aimed at purifying the nanoparticles. It involves thorough cleaning to remove any unnecessary residues, ensuring that the nanoparticles are free from aggregates and extraneous materials that could interfere with subsequent characterization and applications.

(5) **Optional Nitrogen, Oxygen or Argon Annealing**

- Prior to annealing, we prepare our samples by placing a measured portion, typically between 15-20 mg, on gold sheets. These samples are then posi-

tioned in an alumina crucible inside the furnace, ensuring they are ready for the thermal process.

- During annealing, we subject the samples to a controlled environment by inducing a gas flow of either nitrogen, oxygen, or argon at a rate of 100 cubic centimeters per minute. The furnace temperature is initially set at 21°C and is increased at a constant rate of 3°C/min until reaching 150°C. The temperature is maintained at 150°C for 180 minutes to ensure thorough annealing. After completion, the furnace is allowed to cool back to room temperature.

(6) **Physical Property Measurement System (PPMS)**

- The Physical Property Measurement System (PPMS) is utilized to measure the magnetic moment's response to an applied magnetic field, post-demagnetization of the sample. Through this measurement, we obtain the hysteresis loops, which are of tremendous value. These loops play a critical role in our analysis, as they enable the algorithm to correlate the magnetic properties with Scanning Electron Microscopy (SEM) and Powder X-ray Diffraction (PXRD) data, providing a comprehensive mapping of the material's characteristics.
- While our primary focus lies on interpreting the algorithm's results, it is essential not to overlook the physical implications of the actual hysteresis loops. The coercivity, indicated by the width of the loops, and the sat-

uration magnetization, reflected by their height, are critical parameters. These values provide insight into the magnetic hardness and the magnetic moment capacity of the material, respectively, and are indispensable for a comprehensive understanding of the sample's magnetic properties.

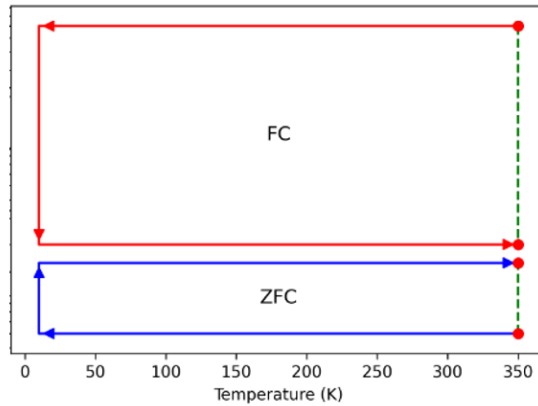


Figure 5.2: Demagnetization sequence, and magnetization for Hysteresis measurement.

(7) PXR D Measurements

- We prepare our samples for PXR D analysis by employing a dropcasting technique. Using a pipette and isopropyl alcohol (IPA), we distribute the sample into the powder holder, aiming for uniform dispersion across the surface. The sample is then allowed to dry for a few minutes.
- The range of interest for our measurements spans from 10 degrees to 90 degrees in two theta. We utilize a divergence slit of 0.6mm and an air scatter slit of 1mm to optimize the precision of our diffraction data.

- We used a D2 PHASER machine. The parameters for our measurements are set as follows: Voltage (V) = 30 kV, Current (I) = 10 mA, Power (P) = 300W. The tube wavelength (λ) is 1.54184 Å. We configure the upper voltage discriminator at 0.25V and the lower voltage discriminator at 0.14V. The time step is set at 0.500 seconds resulting in 2635 steps, with a delta theta of 0.0303673 degrees and a PSD opening of 4.85 degrees.
- After acquisition, we save the diffraction data and utilize Profex software for peak detection and analysis.
- The identified peaks are subsequently processed through an algorithm that calculates nanoparticle sizes, crystallinity, and the percentage of amorphous material in the sample.

(8) SEM Measurements

- For SEM and EDS measurements, we typically use less than five milligrams of the sample. Our instrument, the Axia ChemiSEM, features a high-performance thermal emission SEM column with dual-anode source emission geometry and fixed objective aperture. It includes through-the-lens differential pumping and is enhanced by automation technologies like SmartAlign and live quantitative EDS mapping, offering a superior user experience.
- Our measurement parameters are set as follows: The electron beam resolution is 500 nm at 30 kV in Secondary Electron mode (SE) and in low

vacuum conditions. The spot size can vary between 2.0 to 4.5, depending on the sample. We adhere to the recommended settings provided by the engineering department to ensure optimal resolution and efficient use of the instrument.

- In addition to SEM, we perform EDS and CBS (Channeling Backscatter Spectroscopy) to conduct elemental analysis of the materials. These analyses allow us to map the elemental composition to the actual area of the captured image. This mapping provides insights into the porosity and density of the materials. Moreover, when the resolution is sufficient, it enables us to observe the morphology and layer structure of the samples.

(9) **TEM Measurements**

- The TEM instrument features computer-controlled operations, offering a resolution up to 3 Angstroms and a magnification capability up to 370,000 times. This high level of detail makes it suitable for collecting data necessary for 3D reconstructions of negative-stained samples.
- We collaborate with Penn State for the execution of our TEM analyses. The analyses focus on several key aspects of the samples, including layer composition, edge morphology, and porosity maps. These detailed measurements allow for a comprehensive understanding of the material properties and structural characteristics.

Laboratory Instruments/Equipment



Figure 5.3: Laboratory pictures from left to right: PPMS, scale, sealing machinery, torch, furnace.

CHAPTER 6

Results

In this chapter, we present a detailed analysis of both experimental results and simulations, systematically divided into four distinct sections to comprehensively explore the properties of the synthesized nanoparticles. The first section delves into the magnetic properties of the nanoparticles, utilizing a Physical Property Measurement System (PPMS) to elucidate their magnetic characteristics. The second section focuses on size characterization through Powder X-ray Diffraction (PXRD), which also provides insights into the crystallinity and amorphous nature of the samples. The third section integrates Scanning Electron Microscopy (SEM) results with Energy Dispersive Spectroscopy (EDS) mapping, offering a detailed account of the elemental composition and distribution within the nanoparticles. Finally, the fourth section presents Transmission Electron Microscopy (TEM) analyses conducted by our proprietary algorithm, which categorizes the nanoparticles based on size, shape, layering, and types of junctions. This structured approach allows for a thorough and systematic presentation of the data, facilitating a deeper understanding of the synthesized nanoparticles' physical and chemical properties.

6.1 Magnetic Properties from PPMS Data

The following results were measured using a Vibrating Sample Magnetometer (VSM) which enables the PPMS to operate as a sensitive magnetometer. This section presents results as follows:

- Carbon-based samples (Pc, TPP, and TCPP) subjected to pyrolysis conditions with a temperature of 900°C and a duration of 10 minutes: Magnetic remanence, saturation, and coercivity from hysteresis loops. These carbon matrices were measured at different temperatures ranging from 5K to 300K. Annealing treatments started at 20°C, with a rate of temperature increase of 3°C/min, and were maintained at 150°C for 180 minutes under Nitrogen, Oxygen, and Argon gases. Results are shown for temperatures of 10K and 300K.
- Nanoparticle samples (FePc, FeTCPP, and FeTPP) with different pyrolysis conditions, all at a temperature of 900°C for 60, 120, and 180 minutes. These nanoparticles were measured at 10K and 300K to capture their magnetic remanence, saturation, and coercivity from hysteresis loops. Conditions involving Nitrogen and Oxygen were tested as previously mentioned for the carbon matrices. Additionally, the blocking temperature was determined from zero field cooling and field cooling sequences at low magnetic field ($H = 1$ kOe) and high magnetic field ($H = 60$ kOe) from 10K to 300K.

6.1.1 Noise Treatment for TPP, TCPP, and Pc Matrices

During the measurement of the unnormalized magnetic moments of carbon matrices, values were typically in the order of 10^{-6} emu. Given that these measurements were conducted up to a magnetic field strength of 20 kOe, the proximity of the measured moments to the noise floor of the system becomes a significant consideration.

The Vibrating Sample Magnetometer (VSM) used in our experiments has a noise floor of less than 6.0×10^{-7} emu at 300 K, with additional relative noise levels contributing 3.0×10^{-7} emu/T. This indicates that the smallest detectable signal by the VSM approaches the scale of the magnetic moments we observed in the carbon matrices. Such a scenario suggests that the precision of our magnetic measurements is bounded by the inherent noise characteristics and sensitivity limits of the VSM equipment.

6.1.2 Software Approach to Managing Measurement Noise

To manage and mitigate the effects of noise on the measurement data, a specialized data processing approach was developed and implemented. This approach includes a series of steps designed to normalize and smooth the magnetic moment data extracted from experimental results. This is particularly crucial for enhancing the signal-to-noise ratio, which directly impacts the reliability and accuracy of our findings.

Normalization of Magnetic Moments

The magnetic moment data are normalized against the mass of the samples, providing a clearer comparison by scaling the moments to a standard reference value (per gram of sample). This normalization is essential for evaluating and comparing the intrinsic magnetic properties of the carbon matrices irrespective of sample size or mass differences.

Smoothing of Data

To further refine our measurements and reduce the impact of random noise fluctuations, a smoothing algorithm known as the Savitzky-Golay filter is applied to the normalized data. This filter is particularly effective for noisy data as it helps in preserving the high-frequency components of the measurement signal (features like peaks and troughs) while reducing noise. It works by fitting successive sub-sets of adjacent data points with a low-degree polynomial by the method of linear least squares. When the data points are fitted to the polynomial, the filter evaluates the polynomial at the central point of each subset, which serves as the smoothed data point.

This smoothing process not only helps in dampening the noise but also in clarifying the true underlying trends in the magnetic properties of the samples. It is particularly valuable when dealing with low magnetic moments that are close to the noise floor of the measurement system, as it enhances the detectability of subtle changes in the magnetic response under different experimental conditions.

Implications of Noise and Measurement Sensitivity

Given the fine margins between the magnetic moments of the samples and the machine's noise floor, it is conceivable that the accuracy of measurements for low-magnetic-moment materials like carbon matrices could be influenced predominantly by the machine's limitations. The ability to differentiate between the actual magnetic signal from the sample and the background noise becomes less distinct as the signal approaches the noise floor, implying that:

- **Signal-to-Noise Ratio:** The effective signal-to-noise ratio in our measurements is crucial, particularly when analyzing materials that exhibit weak magnetic properties. Enhancing this ratio is key to improving the reliability of our results.
- **Measurement Thresholds:** The closeness of the observed magnetic moments to the noise floor underscores the importance of considering measurement thresholds when interpreting the magnetic properties of carbon matrices. This also highlights the potential for measurement artifacts or errors introduced by slight fluctuations in the machine's performance or environmental conditions.
- **Operational Parameters:** Adjustments in operational parameters, such as oscillation amplitude and frequency as well as averaging times, might be necessary to optimize measurements and reduce the impact of noise, especially in the range close to the system's noise floor.

6.1.3 Influence of Graphene Planes Orientation and Diamagnetism on Noise

The precision of magnetic moment measurements in carbon matrices is also affected by the intrinsic properties of the graphene planes given by the different phases during pyrolysis in the experiments. According to Lin et al. (2017), the orientation control of graphene planes by magnetic fields significantly influences their diamagnetic responses, which can contribute to noise in magnetic measurements [Lin et al., 2017].

Monolayer vs. Multilayer Graphene Planes Graphene planes, depending on their number of layers, exhibit varying degrees of diamagnetism, which is crucial for their orientation in magnetic fields. The study demonstrates that few-layer graphene planes exhibit a higher diamagnetic susceptibility compared to multilayer planes [Lin et al., 2017]. This difference in susceptibility leads to different orientation behaviors under magnetic fields, thereby affecting the magnetic response measured.

Impact on Measurement Noise The orientation of graphene planes relative to the applied magnetic field can induce variations in the measured magnetic moments. As planes align with the field, their magnetic properties might appear amplified or diminished depending on their angle of orientation, contributing to the noise in the measurement data. In the context of our experiments, where precise measurement of weak magnetic signals is crucial, the inherent noise from plane orientation could be a significant factor. The paper by Lin et al. highlights the potential for orientation-dependent variations to contribute to the overall noise observed in

magnetic measurements of carbon matrices, where graphene planes are utilized.

For detailed study on the alignment and its effects on the magnetic properties, Lin et al.'s work provides an essential insight into how the physical characteristics of graphene can influence experimental outcomes in magnetic field applications. This is particularly relevant when considering the minute magnetic moments typical of diamagnetic materials like graphene, where measurement sensitivity is near the noise floor of the analytical equipment [Lin et al., 2017].

Pc Results

In examining the magnetic properties of the first precursor for the carbon matrices, Phthalocyanine (Pc) demonstrated a distinct diamagnetic behavior in the VSM measurements conducted at 300K, as illustrated in Figure 6.1. A significant observation from these measurements is the pronounced effect of nitrogen annealing, which appears to decrease the saturation magnetization of the sample. This reduction can be attributed to the removal of nitrogen vacancies during the initial pyrolysis process, followed by their re-incorporation into the complex during subsequent annealing.

Furthermore, measurements conducted at 10K reveal that the sample exhibits superparamagnetic behavior, which is typical at low temperatures. Interestingly, nitrogen annealing also seems to diminish the magnetic saturation at this temperature. The main magnetic parameters of these observations are summarized in Table 6.1.

Optimal conditions for maximizing the $\frac{M_r}{M_s}$ ratio were identified as pyrolysis at 900°C for 10 minutes, with measurements of the magnetic moment at 300K resulting

in an $\frac{M_r}{M_s}$ ratio of 0.067. Conversely, the least favorable conditions were found to be pyrolysis at the same temperature and duration, followed by oxygen annealing, with measurements at 10K yielding an $\frac{M_r}{M_s}$ ratio of 0.046.

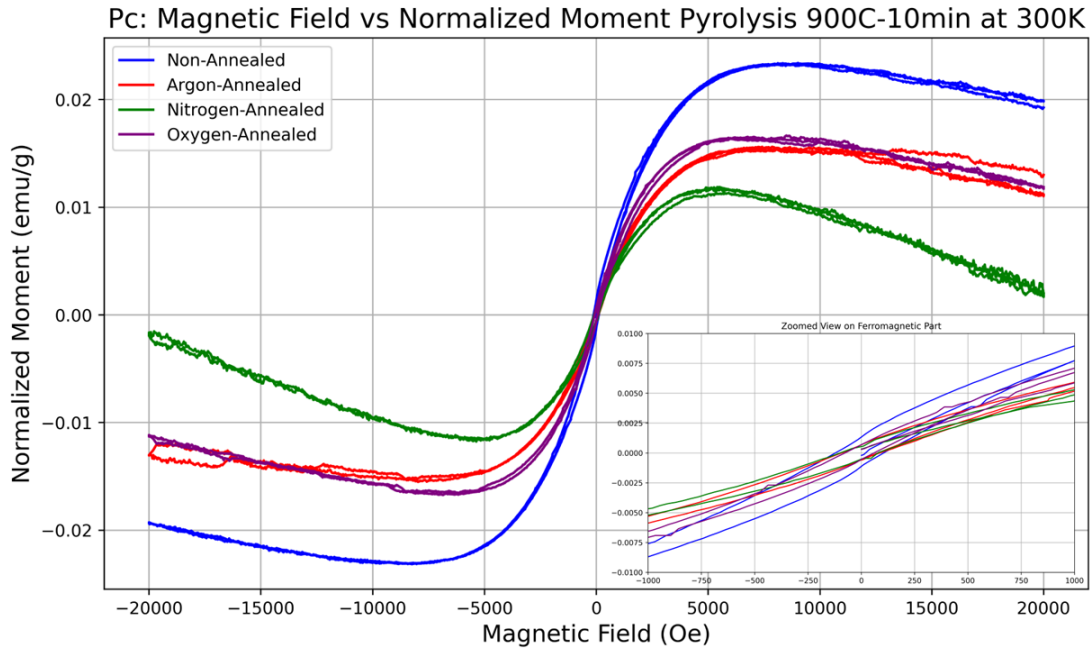


Figure 6.1: All hysteresis loops for samples with pyrolysis at 900C for 10 minutes, measuring magnetic moment at 300K with a maximum applied field of $H = 20\text{kOe}$.

Inset shows the ferromagnetic region of the loops. Source: Vicente Pena Perez

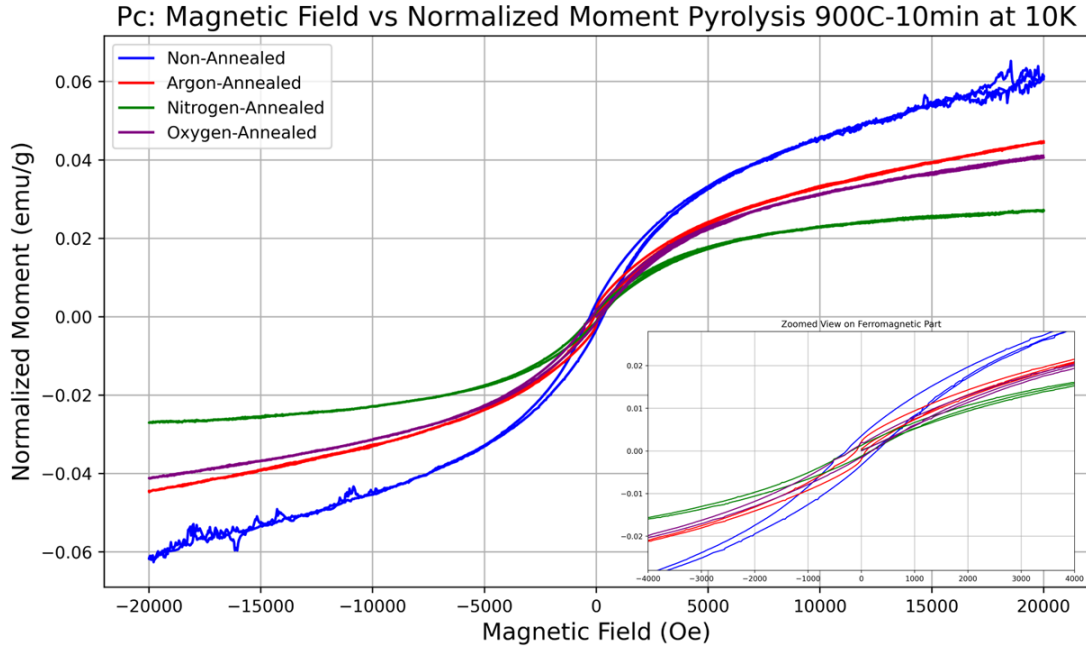


Figure 6.2: All hysteresis loops for samples with pyrolysis at 900C for 10 minutes, measuring magnetic moment at 10K with a maximum applied field of $H = 20\text{kOe}$.

Inset shows the ferromagnetic region of the loops. Source: Vicente Pena Perez

Conditions 900C-10min	M_s (emu/g)	H_c (Oe)	M_r (emu/g)	M_r/M_s	Area (Oe*emu/g)
300K	0.023	99.24	0.0015	0.067	10.45
300K Oxygen	0.016	75.82	0.0010	0.061	7.44
10K	0.061	309.92	0.0037	0.061	48.24
10K Argon	0.044716	88.64	0.0024	0.055	22.40
300K Nitrogen	0.011935	98.318	0.00063	0.053	5.38
300K Argon	0.015560	77.065	0.00076	0.049	4.51
10K Nitrogen	0.027099	178.17	0.0013	0.048	21.89
10K Oxygen	0.041133	199.34	0.0019	0.046	16.08

Table 6.1: Magnetic Properties of Pc Samples Processed Under Different Conditions

TPP Results

For the second precursor in the study of carbon matrices, Tetraphenylporphyrin (TPP) exhibited the most pronounced diamagnetic behavior. As demonstrated in Figure 6.3, the measurements at 300K indicate that oxygen annealing significantly influences the magnetic saturation. Specifically, the oxygen-annealed sample shows a notable decrease in diamagnetism or an increase in paramagnetism, suggesting that the TPP matrix is highly sensitive to the presence of oxygen. Further analysis at 10K, shown in Figure 6.4, reveals the expected superparamagnetic behavior. The presence of oxygen again plays a crucial role, enhancing the superparamagnetic response of the sample. Moreover, Figure 6.5 illustrates the transition in magnetic moments from 300K to 5K. This transition clearly showcases the behavior of the oxygen-annealed sample shifting from nearly diamagnetic at higher temperatures to distinctly superparamagnetic at lower temperatures. Finally, as summarized in Table 6.2, the optimal conditions for maximizing the $\frac{M_r}{M_s}$ ratio were identified as pyrolysis at 900°C for 10 minutes, with magnetic moment measurements at 10K yielding an $\frac{M_r}{M_s}$ ratio of 0.11. Conversely, the least favorable conditions involved pyrolysis at the same temperature and duration, followed by oxygen annealing, with measurements at 300K resulting in an $\frac{M_r}{M_s}$ ratio of 0.0081.

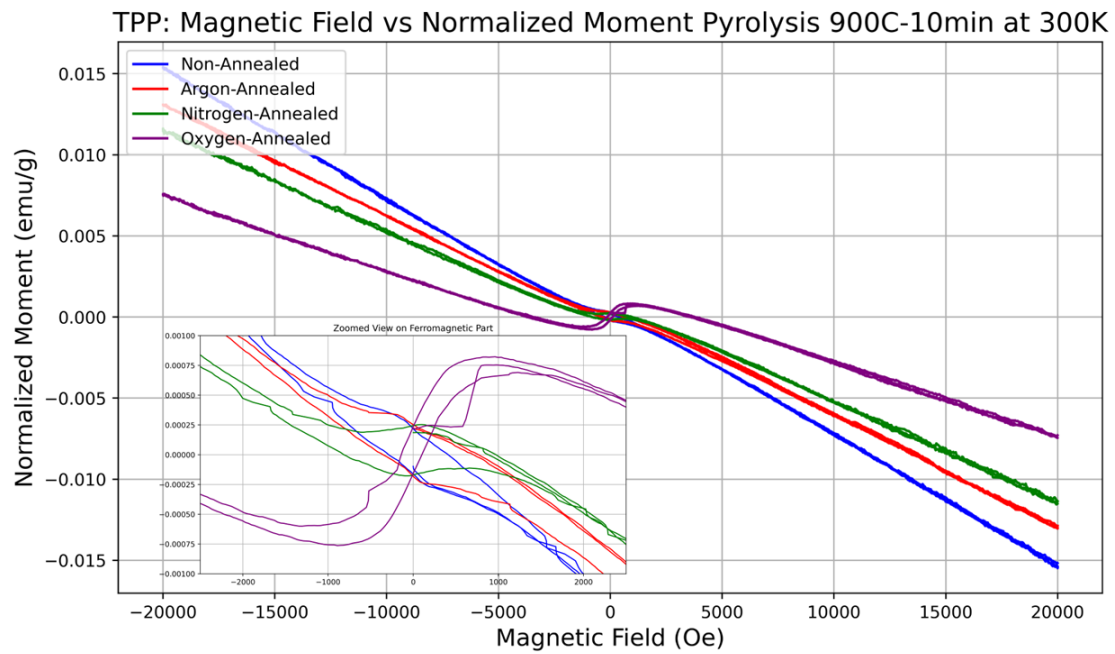


Figure 6.3: All hysteresis loops for samples with pyrolysis at 900C for 10 minutes, measuring magnetic moment at 300K with a maximum applied field of $H = 20\text{kOe}$.

Inset shows the ferromagnetic region of the loops. Source: Vicente Pena Perez

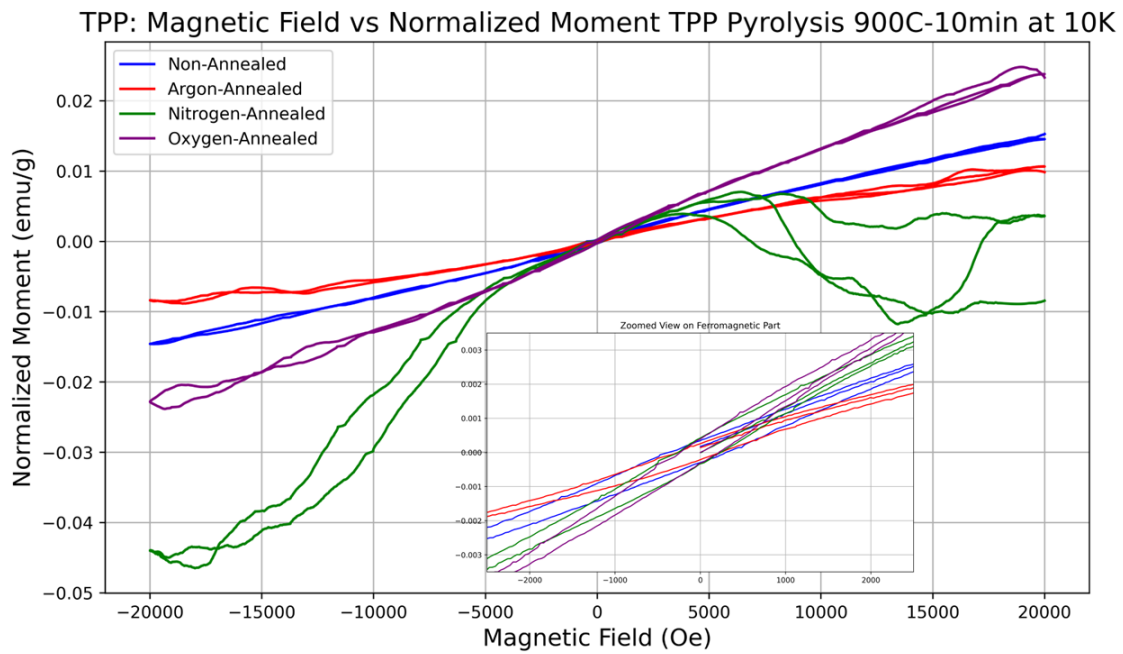


Figure 6.4: All hysteresis loops for samples with pyrolysis at 900C for 10 minutes, measuring magnetic moment at 10K with a maximum applied field of $H = 20\text{kOe}$.

Inset shows the ferromagnetic region of the loops. Source: Vicente Pena Perez

TPP: Magnetic Field vs Normalized Moment Pyrolyzed & Oxygen Annealed 150C-180min

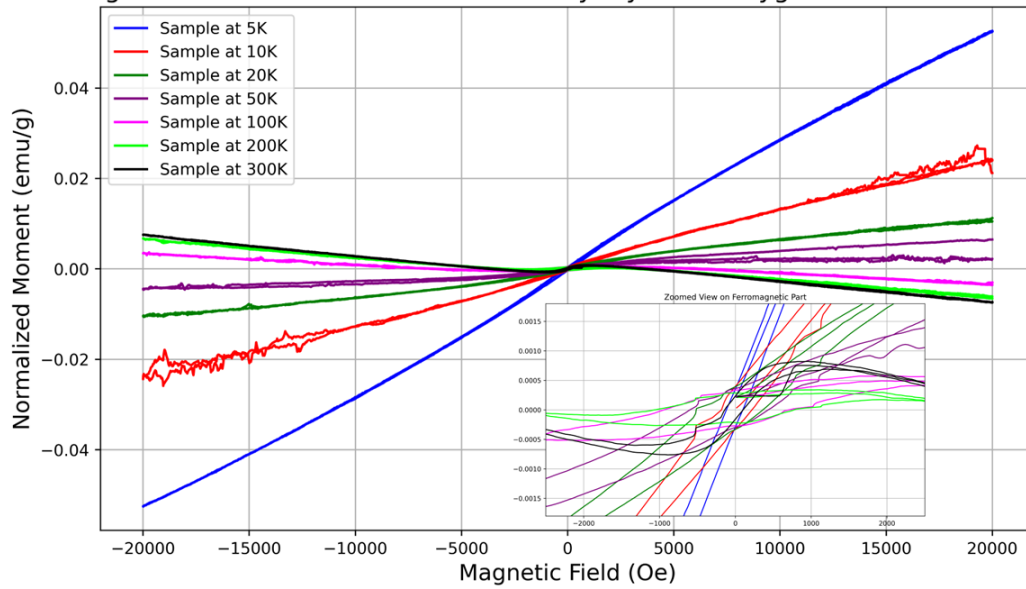


Figure 6.5: All hysteresis loops for samples with pyrolysis at 900C for 10 minutes and oxygen annealed at 150C for 180 minutes, measuring magnetic moment in the range 5K to 300K with a maximum applied field of $H = 20\text{kOe}$. Inset shows the ferromagnetic region of the loops. Source: Vicente Pena Perez

Conditions 900C-10min	Ms (emu/g)	Hc (Oe)	Mr (emu/g)	Mr/Ms	Area (Oe*emu/g)
10K Nitrogen	0.0055	254.13	0.00066	0.11	6.42
100K Oxygen	0.0034	953.54	0.00025	0.074	4.97
50K Oxygen	0.0065	442.95	0.00040	0.0625	4.25
200K Oxygen	0.0066	1152.88	0.00031	0.047	8.75
20K Oxygen	0.011	355.12	0.00043	0.038	3.31
10K	0.015	300.042	0.00044	0.028	4.71
10K Argon	0.010	210.40	0.00030	0.028	6.14
10K Oxygen	0.026	210.42	0.00055	0.020	16.89
300K Oxygen	0.0075	177.16	0.00013	0.017	5.59
300K Nitrogen	0.011	776.15	0.00016	0.014	1.18
300K Argon	0.013	375.099	0.00016	0.012	5.53
5K Oxygen	0.052	78.46	0.00056	0.010	24.88
300K	0.015	298.26	0.00012	0.0081	0.094

Table 6.2: Magnetic Properties of TPP Samples under Various Conditions

TCPP Results

The final precursor in our study, Tetrakis(4-carboxyphenyl)porphyrin (TCPP), exhibited slightly less diamagnetic behavior compared to Tetraphenylporphyrin (TPP). This difference is evident from Figure 6.6, where an analysis of the noise was conducted on two identical samples that underwent the same initial pyrolysis conditions. Due to the sensitivity of the Vibrating Sample Magnetometer (VSM), significant noise was observed. Among these, Sample 2 demonstrated greater stability and was thus selected for further analysis. Comparisons against annealed versions of TCPP, particularly the oxygen-annealed variant, are shown in Figure 6.7. The oxygen-annealed sample exhibited a significant increase in magnetic saturation, indicating a pronounced response to oxygen treatment. The sensitivity of TCPP to lower tem-

peratures was further highlighted in Figure 6.8. Remarkably, it was conjectured that the sample exhibits layer-wise temperature dependence, with more noise observed at lower temperatures due to the layers behaving more like monolayers than multilayers, as is typical at higher temperatures. This temperature dependency significantly impacts the overall magnetization, transitioning from superparamagnetic to superdiamagnetic properties. Interestingly, as shown in Figure 6.9, oxygen treatment appears to improve this noise issue, suggesting that it introduces some stability to the layers. Moreover, the temperature dependence of the TCPP matrix from a high temperature of 300K to a lower one of 5K is depicted in Figure 6.10, showing a nice transition in magnetic properties. Finally, as summarized in Table 6.3, the optimal conditions for maximizing the $\frac{M_r}{M_s}$ ratio were identified as pyrolysis at 900°C for 10 minutes, with magnetic moment measurements at 20K yielding an $\frac{M_r}{M_s}$ ratio of 1.59. Conversely, the least favorable conditions involved pyrolysis at the same temperature and duration, followed by nitrogen annealing, with measurements at 300K resulting in an $\frac{M_r}{M_s}$ ratio of 0.0084.

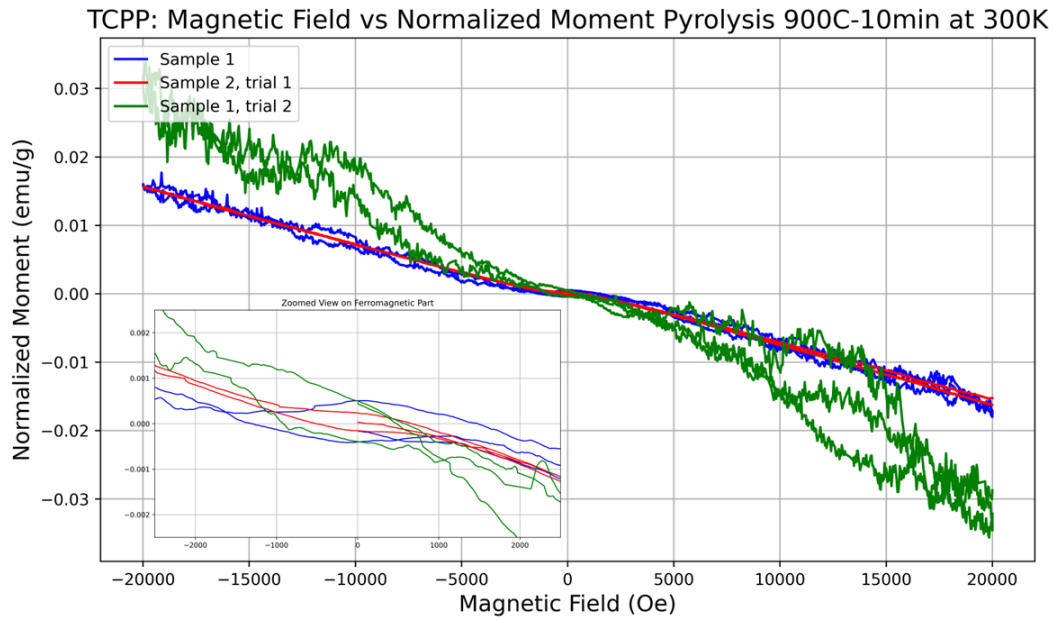


Figure 6.6: Hysteresis loops for two samples with pyrolysis at 900C for 10 minutes, measuring magnetic moment at 300K with a maximum applied field of $H = 20\text{kOe}$.

Inset shows the ferromagnetic region of the loops. Source: Vicente Pena Perez

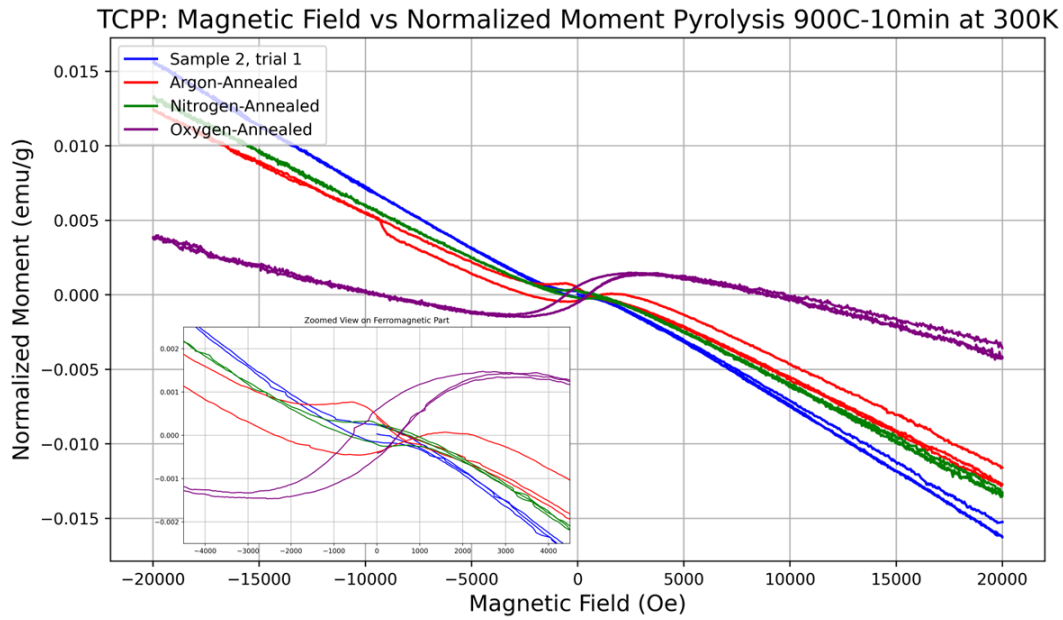


Figure 6.7: All hysteresis loops for samples with pyrolysis at 900C for 10 minutes, measuring magnetic moment at 300K with a maximum applied field of $H = 20\text{kOe}$. Annealing conditions for all were at 150C for 180 minutes. Inset shows the ferromagnetic region of the loops. Source: Vicente Pena Perez

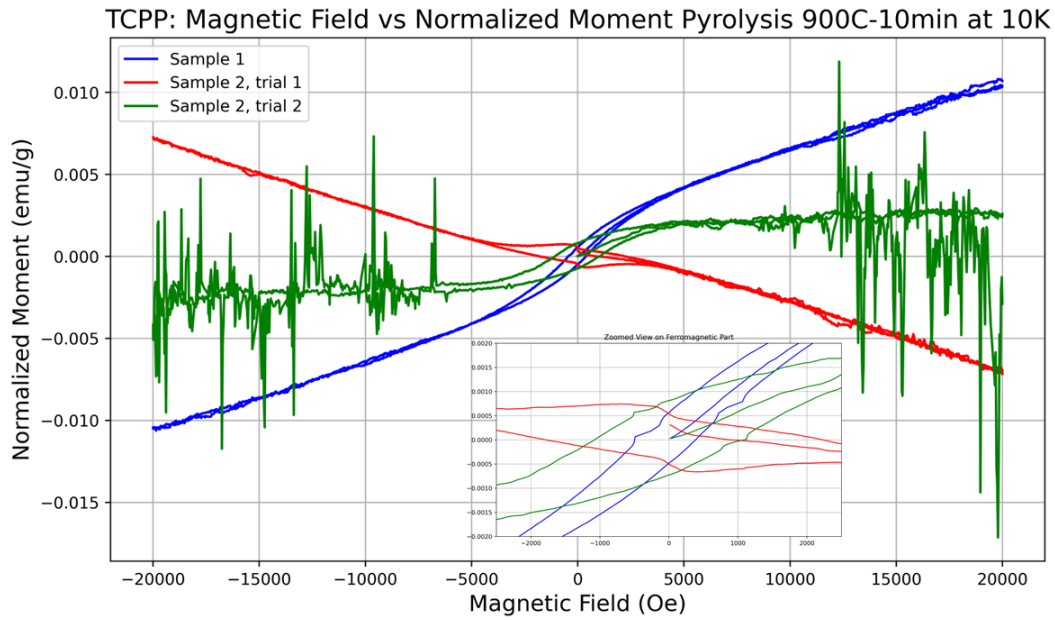


Figure 6.8: Hysteresis loops for two samples with pyrolysis at 900C for 10 minutes, measuring magnetic moment at 10K with a maximum applied field of $H = 20\text{kOe}$.

Inset shows the ferromagnetic region of the loops. Source: Vicente Pena Perez

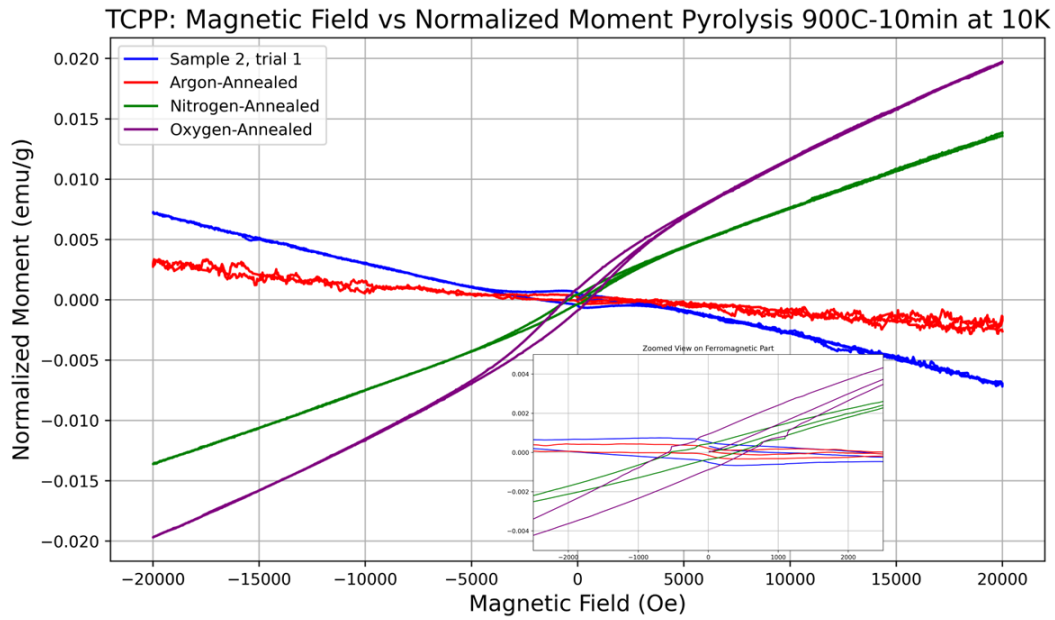


Figure 6.9: All hysteresis loops for samples with pyrolysis at 900C for 10 minutes, measuring magnetic moment at 10K with a maximum applied field of $H = 20\text{kOe}$. Annealing conditions for all were at 150C for 180 minutes. Inset shows the ferromagnetic region of the loops. Source: Vicente Pena Perez

T CPP: Magnetic Field vs Normalized Moment Pyrolyzed & Oxygen Annealed 150C-180min

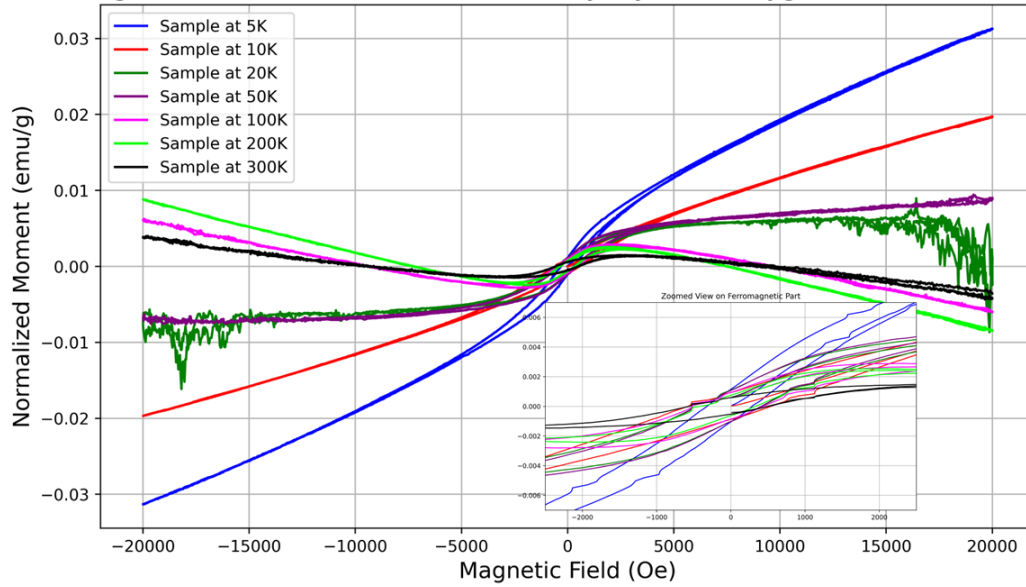


Figure 6.10: All hysteresis loops for samples with pyrolysis at 900C for 10 minutes and oxygen annealed at 150C for 180 minutes, measuring magnetic moment in the range 5K to 300K with a maximum applied field of $H = 20\text{kOe}$. Inset shows the ferromagnetic region of the loops. Source: Vicente Pena Perez

Conditions 900C-10min	Ms (emu/g)	Hc (Oe)	Mr (emu/g)	Mr/Ms	Area (Oe*emu/g)
20K	0.000538	1917.564	0.000858	1.5953	6.628
300K Oxygen	0.001489	488.133	0.000593	0.3986	3.129
10K	0.002514	1063.437	0.000850	0.3381	13.776
100K Oxygen	0.002905	409.621	0.000940	0.3235	7.223
200K Oxygen	0.002597	323.806	0.000812	0.3127	4.393
5K	0.003594	599.913	0.000882	0.2454	6.715
50K	0.003598	3482.440	0.000649	0.1804	7.902
20K Oxygen	0.006398	409.731	0.001108	0.1733	12.752
50K Oxygen	0.008915	399.334	0.001090	0.1223	13.698
10K	0.007225	1785.438	0.000509	0.0704	6.828
10K Oxygen	0.019852	532.448	0.001159	0.0584	12.372
10K	0.010747	386.310	0.000584	0.0543	6.655
10K Argonn	0.002934	1363.463	0.000159	0.0540	4.706
100K	0.010877	1707.473	0.000564	0.0519	3.530
10K Nitrogen	0.013941	410.459	0.000590	0.0424	7.922
5K Oxygen	0.031317	288.784	0.001295	0.0413	20.097
200K	0.015629	1917.507	0.000475	0.0304	10.774
300K	0.015794	1230.183	0.000434	0.0275	5.982
300K Argon	0.012456	2318.856	0.000304	0.0244	11.948
300K	0.015681	463.947	0.000289	0.0184	0.926
300K	0.032268	943.814	0.000510	0.0158	10.170
5K	0.032521	65.922	0.000378	0.0116	28.613
300K Nitrogen	0.013321	698.128	0.000112	0.0084	3.259

Table 6.3: Magnetic Properties of TCPP Samples under Various Conditions

TCPP:TPP Different Concentration Results

We explored various concentrations of Tetrakis(4-carboxyphenyl)porphyrin (TCPP) and Tetraphenylporphyrin (TPP) to identify a stability point between the two matrices. The concentrations tested included 25% TCPP with 75% TPP, 50% TCPP with 50% TPP, and 75% TCPP with 25% TPP, under the original pyrolysis conditions of 900°C for 10 minutes. Figure 6.12 displays the magnetic behavior of these blends

measured at a VSM temperature of 300K. Given the low magnetic moment orders, we applied a noise analysis function to these results. The most stable combination at 300K was found to be 75% TCPP with 25% TPP. Further analysis at 10K, presented in Figure 6.11, revealed that the least stable concentration was 50% TCPP with 50% TPP. However, the best in terms of magnetic saturation was the blend with 25% TCPP and 75% TPP, while the best based on coercivity was 75% TCPP with 25% TPP. We also explored the effects of oxygen annealing on these concentrations at low temperatures. As shown in Figure 6.13, all the concentrations maintained superdiamagnetic behavior even under these conditions. The best sample was consistently 25% TCPP with 75% TPP. Lastly, as summarized in Table 6.4, the optimal conditions for maximizing the $\frac{M_r}{M_s}$ ratio were achieved with a mixture of 50% TCPP and 50% TPP at 300K, resulting in an $\frac{M_r}{M_s}$ ratio of 0.54. Conversely, the least favorable conditions involved the same blend ratio measured at 10K, yielding an $\frac{M_r}{M_s}$ ratio of 0.00053.

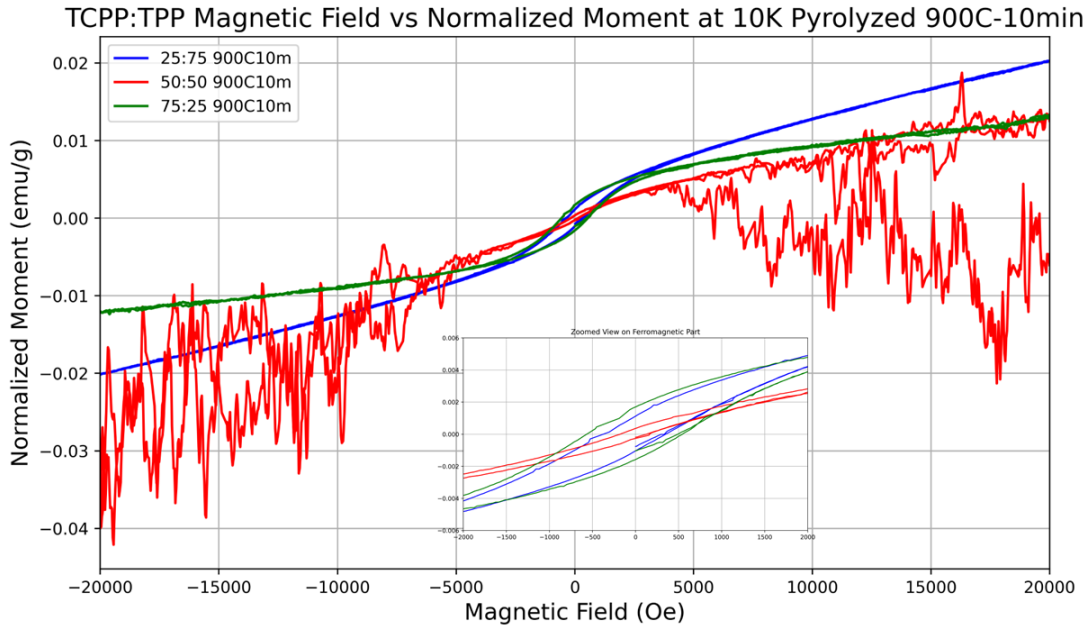


Figure 6.11: Hysteresis loops for different concentration of TCPP and TPP with pyrolysis at 900C for 10 minutes, measuring magnetic moment at 10K with a maximum applied field of $H = 20\text{kOe}$. Inset shows the ferromagnetic region of the loops.

Source: Vicente Pena Perez

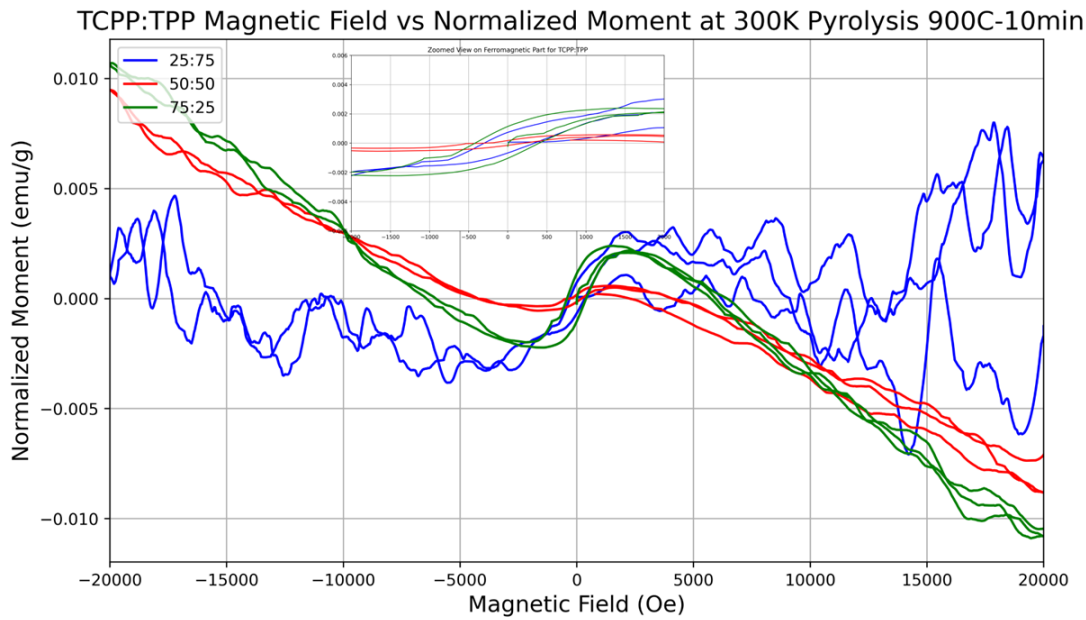


Figure 6.12: Hysteresis loops for different concentration of TCPP and TPP with pyrolysis at 900C for 10 minutes, measuring magnetic moment at 300K with a maximum applied field of $H = 20\text{kOe}$. Inset shows the ferromagnetic region of the loops.

Source: Vicente Pena Perez

TCPP:TPP Magnetic Field vs Normalized Moment Oxygen Annealed & Pyrolysis 900C-10min at 10K

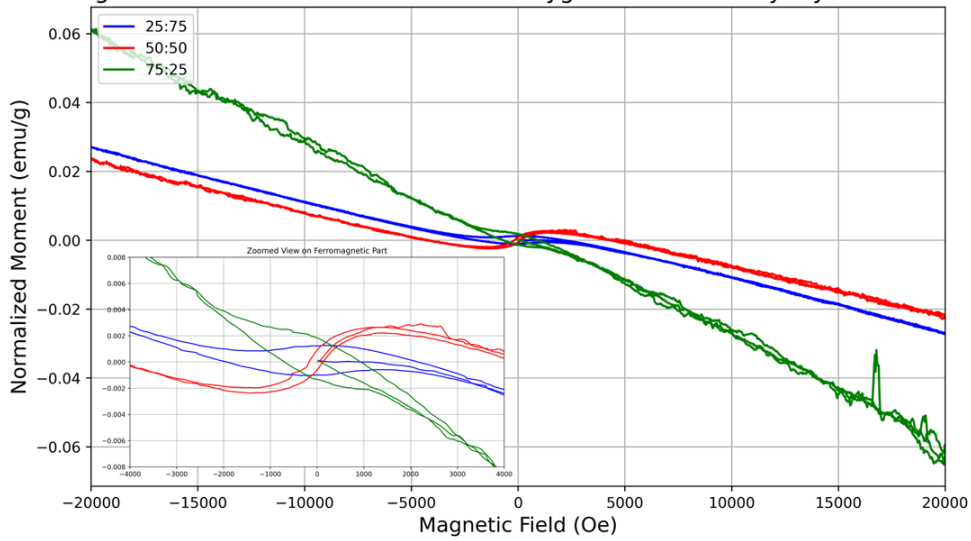


Figure 6.13: Hysteresis loops for different concentration of TCPP and TPP with pyrolysis at 900C for 10 minutes and oxygen annealed at 150C for 180 minutes, measuring magnetic moment at 10K with a maximum applied field of $H = 20\text{kOe}$. Inset shows the ferromagnetic region of the loops. Source: Vicente Pena Perez

Conditions 900C-10min	Ms (emu/g)	Hc (Oe)	Mr (emu/g)	Mr/Ms	Area (Oe*emu/g)
2-TCPP50:TPP50 300K	0.00047	210.17	0.00025	0.54	1.90
TCPP75:TPP25 300K	0.0024	422.81	0.0012	0.49	6.20
2-TCPP75:TPP25 300K	0.0030	420.26	0.0012	0.41	5.08
1-TCPP50:TPP50 300K	0.00064	187.22	0.00025	0.40	1.47
TCPP50:TPP50 10K Oxygen	0.0027	121.92	0.00096	0.35	6.36
TCPP25:TPP75 300K	0.0036	300.75	0.00084	0.22	3.90
TCPP75:TPP25 10K	0.013	545.22	0.0017	0.12	13.69
TCPP25:TPP75 10K	0.020	364.39	0.0011	0.055	1.42
TCPP25:TPP75 10K Oxygen	0.026	2162.16	0.0012	0.047	15.46
TCPP75:TPP25 10K Oxygen	0.061	953.45	0.0019	0.031	16.99
TCPP50:TPP50 10K	0.017	167.37	0.00053	0.030	18.36

Table 6.4: Magnetic Properties of TCPP:TPP Blended Samples under Various Conditions

FePc

Building upon our initial findings with carbon matrices, we further investigated the influence of a metal core agent, specifically targeting carbon-coated nanoparticles with iron cores. Our study first focused on comparing the magnetic properties of these nanoparticles under different pyrolysis durations. Figure 6.14 captures the magnetic results at 300K for three samples subjected to the same pyrolysis temperature of 900°C but varied durations ranging from 60 to 180 minutes. Notably, the sample processed for 120 minutes exhibited the highest magnetic saturation at 300K, while the 60-minute sample demonstrated superior coercivity. Further assessments at 10K (see Figure 6.15) confirmed that the 60-minute pyrolysis duration yielded the most favorable outcomes in terms of overall magnetic properties at lower temperatures.

The comprehensive analysis across two temperatures, 10K and 300K, is displayed in Figure 6.16, which substantiates the 60-minute duration as having the best overall performance. Interestingly, similar to earlier observations in the Pc carbon matrix, nitrogen annealing influenced the saturation properties by filling vacancies in the lattice structure. As shown in Figure 6.17, while most cases displayed a decrease in saturation, the 180-minute pyrolysis sample was an exception, underscoring the critical role of pyrolysis conditions in phase generation during synthesis. This suggests a restriction in pyrolysis times to between 60 and 120 minutes. Moreover, Figure 6.18 illustrates that the 60-minute sample remained the most magnetically saturated after nitrogen annealing. Finally, the summarized results in Table 6.5 indicate that the optimal conditions for maximizing the $\frac{M_r}{M_s}$ ratio were found with the 60-minute pyrolysis sample measured at 10K, achieving an $\frac{M_r}{M_s}$ ratio of 0.32. In contrast, the least favorable conditions were observed with the 180-minute sample measured at 300K, which produced an $\frac{M_r}{M_s}$ ratio of 0.10.

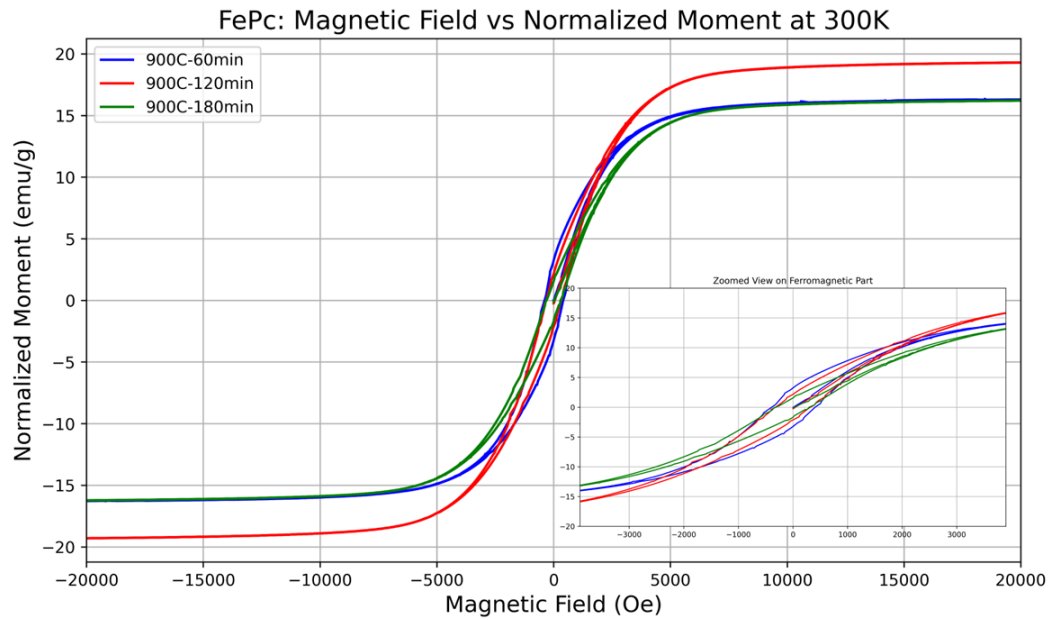


Figure 6.14: All hysteresis loops for FePc with pyrolysis at 900C for different times, measuring magnetic moment at 300K with a maximum applied field of $H = 20\text{kOe}$.

Inset shows the ferromagnetic region of the loops. Source: Vicente Pena Perez

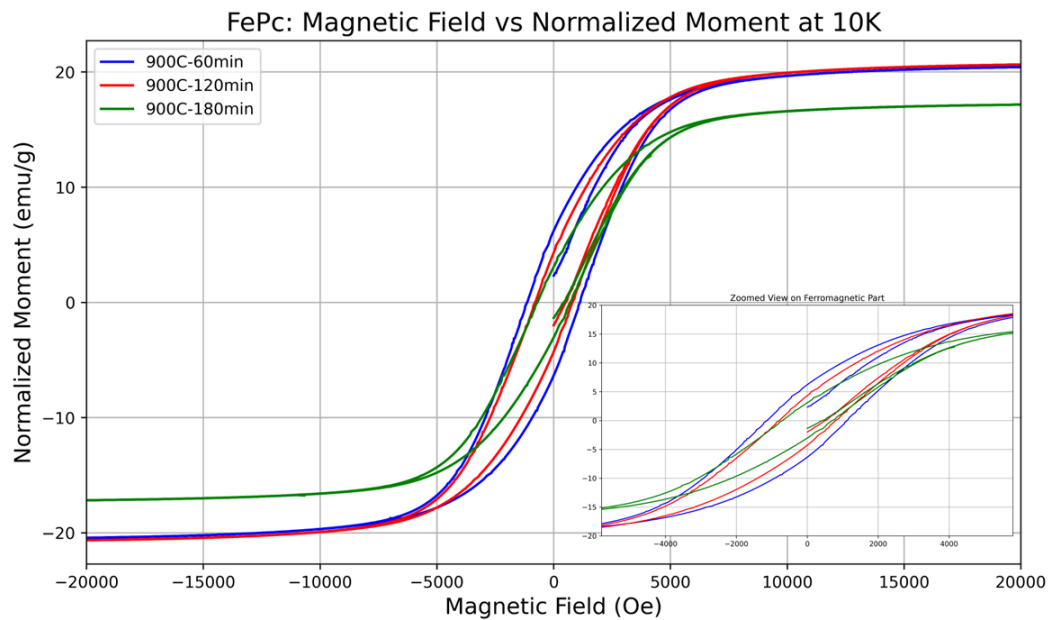


Figure 6.15: All hysteresis loops for FePc with pyrolysis at 900C for different times, measuring magnetic moment at 10K with a maximum applied field of $H = 20\text{kOe}$.

Inset shows the ferromagnetic region of the loops. Source: Vicente Pena Perez

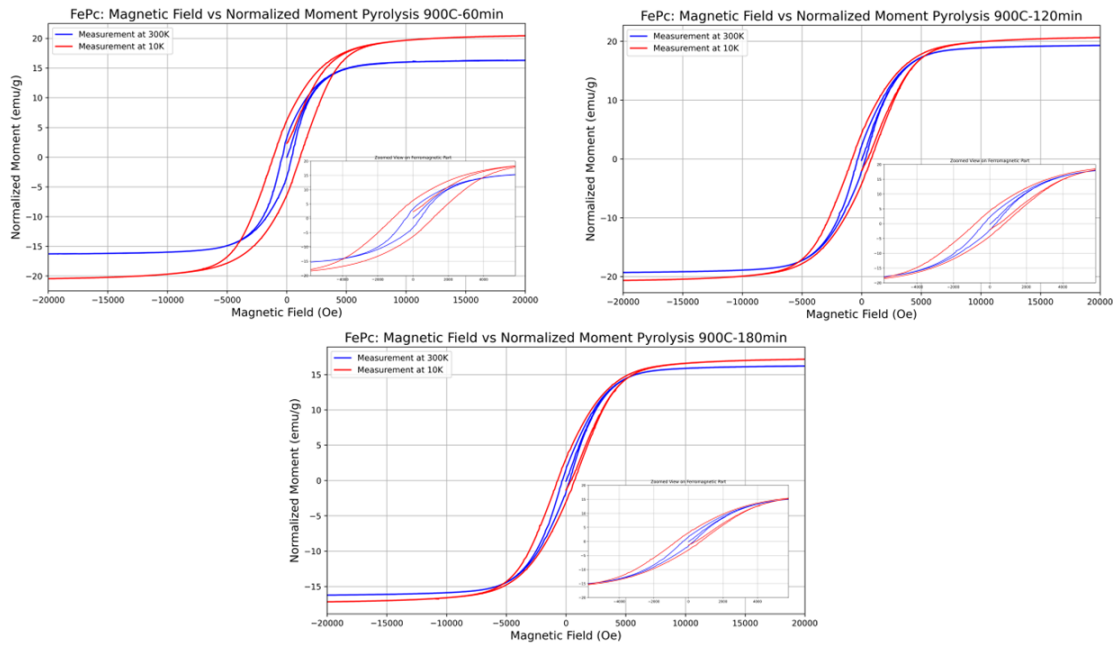


Figure 6.16: All hysteresis loops for FePc with pyrolysis at 900C for different times, measuring magnetic moment at 10K and 300K with a maximum applied field of $H = 20\text{kOe}$. Inset shows the ferromagnetic region of the loops. Source: Vicente Pena Perez

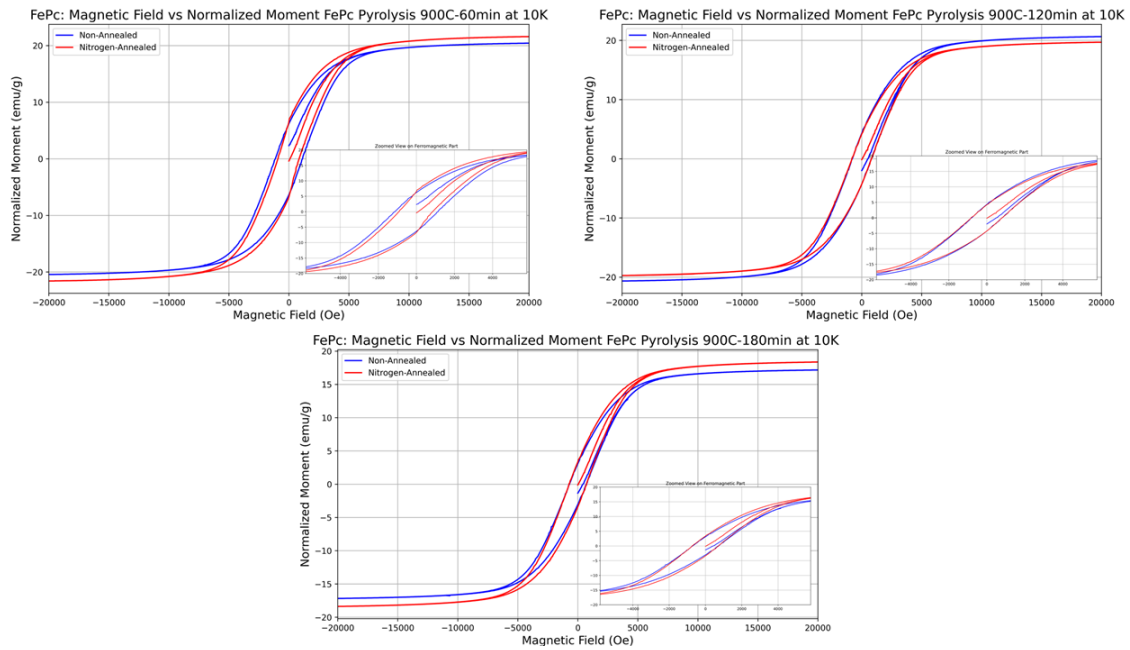


Figure 6.17: All hysteresis loops for FePc with pyrolysis at 900C for different times, measuring magnetic moment at 10K and 300K with a maximum applied field of $H = 20\text{kOe}$. Annealing conditions for all were at 150C for 180 minutes. Inset shows the ferromagnetic region of the loops. Source: Vicente Pena Perez

FePc: Magnetic Field vs Normalized Moment Pyrolyzed & Nitrogen-Annealed 150C-180min

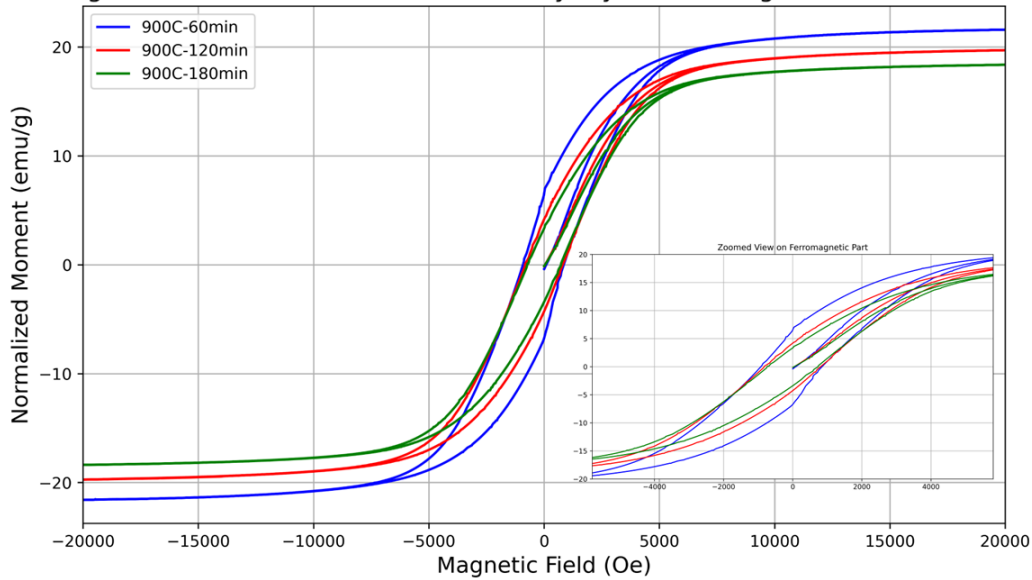


Figure 6.18: All hysteresis loops for FePc with pyrolysis at 900C for different times, measuring magnetic moment at 10K with a maximum applied field of $H = 20\text{kOe}$. Annealing conditions for all were at 150C for 180 minutes. Inset shows the ferromagnetic region of the loops. Source: Vicente Pena Perez

Conditions	Ms (emu/g)	Hc (Oe)	Mr (emu/g)	Mr/Ms	Area (Oe*emu/g)
900C-10min					
10K, 900C-60min	19.66	1154.24	6.29	0.32	70368.57
10K N2, 900C-180min	21.48	842.97	6.75	0.31	37192.75
10K, 900C-120min	20.05	786.98	4.49	0.22	49615.88
10K N2, 900C-120min	19.52	776.32	4.24	0.21	49735.78
300K, 900C-60min	16.09	388.15	3.39	0.21	15647.87
10K, 900C-180min	16.64	689.96	3.14	0.18	34670.40
10K N2, 900C-60min	18.28	732.05	3.32	0.18	65068.34
300K, 900C-120min	18.99	289.34	2.29	0.12	13461.61
300K, 900C-180min	15.85	286.73	1.67	0.10	10258.64

Table 6.5: Magnetic Properties of FePc Samples under Various Conditions

FeTPP

In our examination of FeTPP nanoparticles, we observed intriguing results regarding their magnetic properties. Figure 6.19 illustrates the magnetic behavior of these nanoparticles under different conditions. Table 6.6 summarizes the quantifiable aspects of these properties. The results clearly indicate a negligible coercive field, suggesting that the FeTPP sample exhibits paramagnetic properties, without any ferromagnetic behavior, despite the presence of iron. This is a significant observation as it deviates from expected results given the ferromagnetic nature typically associated with iron-containing compounds. The optimal conditions for maximizing the $\frac{M_r}{M_s}$ ratio were identified as a synthesis duration of 60 minutes at a measurement temperature of 10K, resulting in an $\frac{M_r}{M_s}$ ratio of 0.013. Conversely, the least favorable conditions, involving the same synthesis duration but measured at 300K, yielded an $\frac{M_r}{M_s}$ ratio of 0.0039. These findings suggest that the TPP matrix might require further exploration, potentially with different metals to understand its magnetic behavior comprehensively.

To extend our understanding, colleagues Cristian Reynaga, Erick Villegas, and Sarah Dumont have pursued further studies exploring different metal nanoparticles, suggesting a broader scope of investigation for future research.

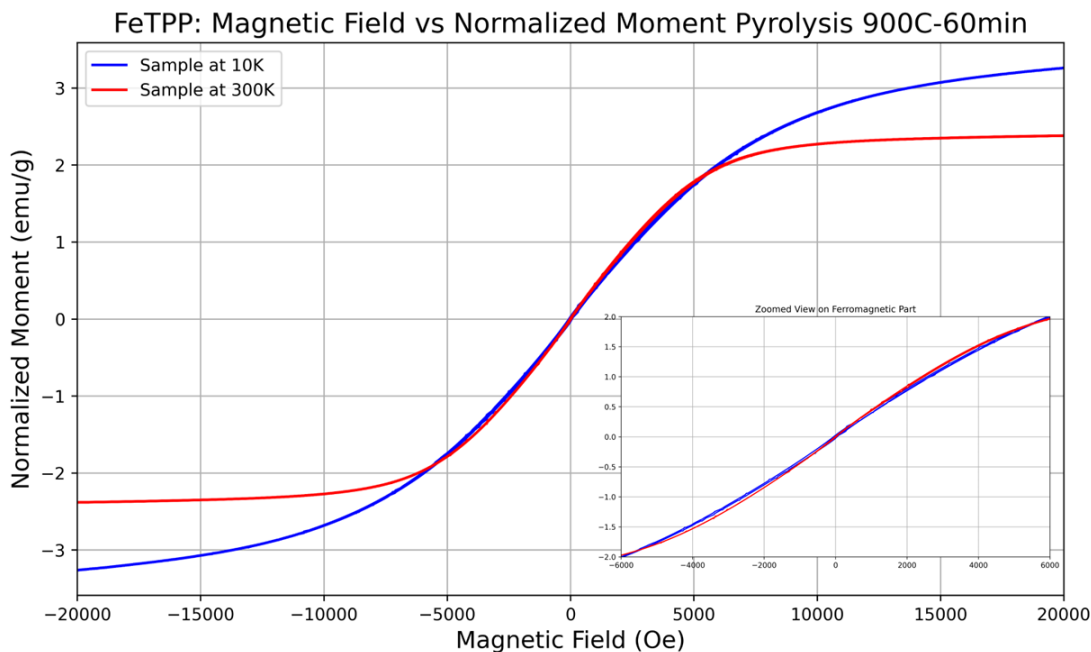


Figure 6.19: All hysteresis loops with pyrolysis at 900C for 60 minutes, measuring magnetic moment at 10K and 300K with a maximum applied field of $H = 20\text{kOe}$.

Inset shows the ferromagnetic region of the loops. Source: Vicente Pena Perez

Conditions	Ms	Hc	Mr	Mr/Ms	Area
900C-10min	(emu/g)	(Oe)	(emu/g)		(Oe*emu/g)
10K, 900C-60min	3.26	33.72	0.045	0.013	1779.52
300K, 900C-60min	2.38	27.99	0.0094	0.0039	172.61

Table 6.6: Magnetic Properties of FeTPP Samples under Various Conditions

FeT CPP

Our exploration concluded with FeT CPP nanoparticles, where Figure 6.20 displays the magnetic measurements at 10K and 300K. Notably, at 10K, there was a significant increase in both saturation and coercivity, demonstrating enhanced magnetic prop-

erties at lower temperatures. Subsequent annealing experiments with nitrogen and oxygen were performed under similar conditions to previous samples. However, as illustrated in Figure 6.21, neither treatment had a substantial effect on the magnetic properties, indicating the stability of the TCPP matrix even when combined with an iron metal core. Further analysis confirmed that the ideal pyrolysis temperature is 900°C with the optimal duration being 60 minutes, as confirmed in Figure 6.22. This setup not only optimized the magnetic properties but also demonstrated the robustness of the synthesis process. Optimal conditions for maximizing the $\frac{M_r}{M_s}$ ratio were determined to be a synthesis duration of 60 minutes at 10K, achieving an $\frac{M_r}{M_s}$ ratio of 0.38. In contrast, the least favorable conditions, with the same duration measured at 300K, produced an $\frac{M_r}{M_s}$ ratio of 0.15. These results underscore the TCPP matrix's exceptional stability under varying annealing conditions and pyrolysis parameters.

Table 6.7

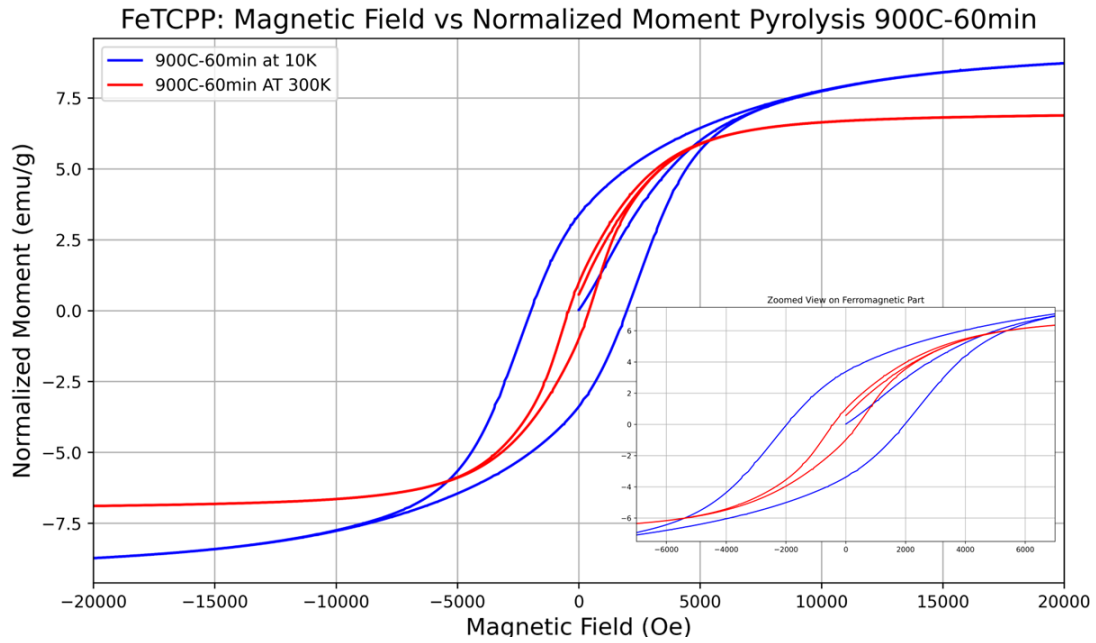


Figure 6.20: All hysteresis loops with pyrolysis at 900C for 60 minutes, measuring magnetic moment at 10K and 300K with a maximum applied field of $H = 20\text{kOe}$.

Inset shows the ferromagnetic region of the loops. Source: Vicente Pena Perez

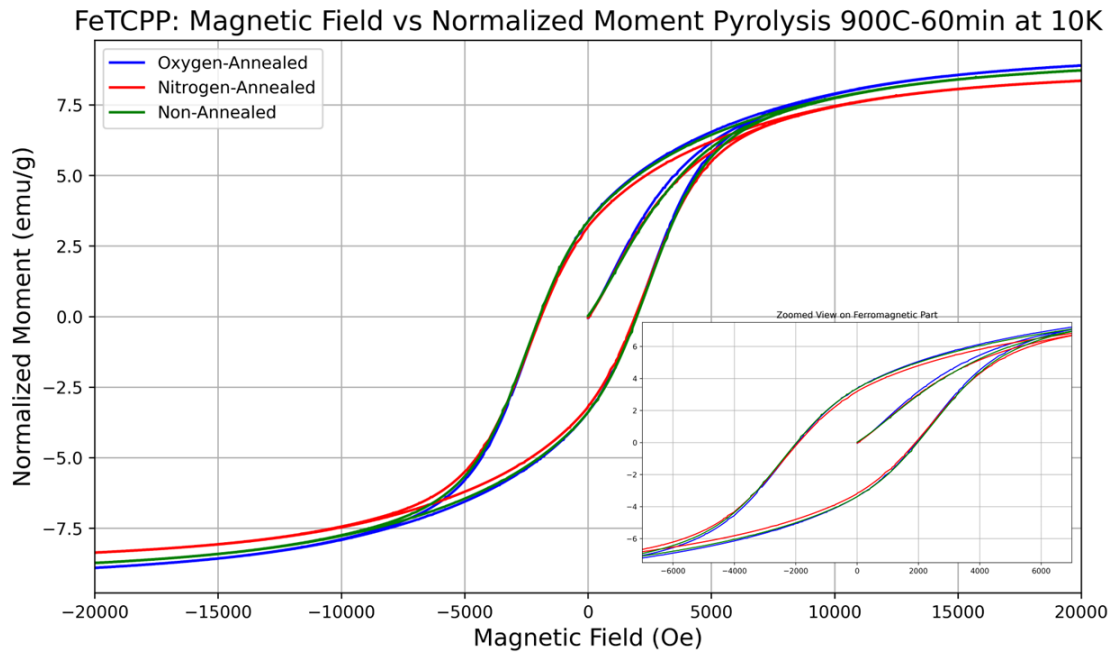


Figure 6.21: All hysteresis loops with pyrolysis at 900C for 60 minutes, measuring magnetic moment at 10K with a maximum applied field of $H = 20\text{kOe}$. Nitrogen and Oxygen annealing are shown with identical conditions 150C for 180 minutes. Inset shows the ferromagnetic region of the loops. Source: Vicente Pena Perez

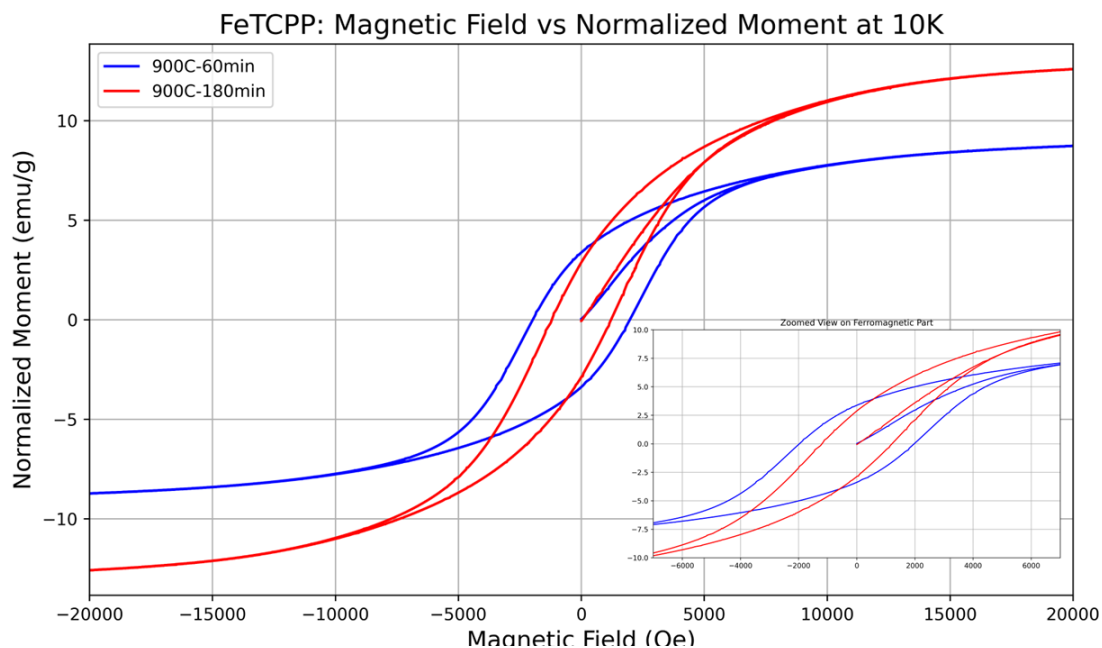


Figure 6.22: All hysteresis loops with pyrolysis at 900C for 60 and 180 minutes, measuring magnetic moment at 10K with a maximum applied field of $H = 20\text{kOe}$.

Inset shows the ferromagnetic region of the loops. Source: Vicente Pena Perez

Conditions	Ms (emu/g)	Hc (Oe)	Mr (emu/g)	Mr/Ms	Area (Oe*emu/g)
900C-10min					
10K, 900C-60min	8.72	1962.71	3.38	0.38	42640.76
10K N2, 900C-60min	8.38	1896.87	3.24	0.38	39719.93
10K O2, 900C-60min	8.91	1919.10	3.42	0.38	43980.13
10K, 900C-180min	12.60	1198.21	2.94	0.23	39914.23
300K, 900C-60min	6.89	409.92	1.04	0.15	7287.85

Table 6.7: Magnetic Properties of FeTCCP Samples under Various Conditions

6.2 PXRD Analyses

This section presents the results of Powder X-ray Diffraction (PXRD) measurements conducted to analyze the structural properties of nanoparticles. The analysis focused on determining average nanoparticle sizes, crystallite sizes, and graphitization indices, along with evaluating the overall crystallinity and graphitization percentages of the samples.

PXRD for Carbon Matrices Pc, TCPP and TPP Results

Given the complexity of the measurements, this section focuses on qualitative analyses of the Powder X-ray Diffraction (PXRD) patterns for the carbon matrices Pc, TCPP, and TPP. This approach allows us to observe fundamental structural differences without delving into quantitative crystallite size calculations. Figure 6.23 shows most prominent difference is the absence of an initial intensity jump in the diffraction pattern of TCPP, which is present in the other matrices. This observation can be inferred as being due to the presence of oxygen, Figure 6.24, within the lattice structure of TCPP, which may influence the degree of structural ordering at certain diffraction angles. This recovery suggests that annealing may facilitate some degree of recrystallization or reordering within the TCPP matrix, potentially by affecting oxygen-related defects or rearrangements in the lattice structure. Such changes are crucial for understanding the structural dynamics under different thermal conditions and their implications for the material properties of TCPP. The qualitative PXRD analysis has provided valuable insights into the structural characteristics of Pc,

TCPP, and TPP matrices, with significant observations on the impact of elemental composition and thermal treatment on the diffraction patterns. Further quantitative studies would be necessary to precisely define the crystallite sizes and detailed crystallographic properties of these materials.

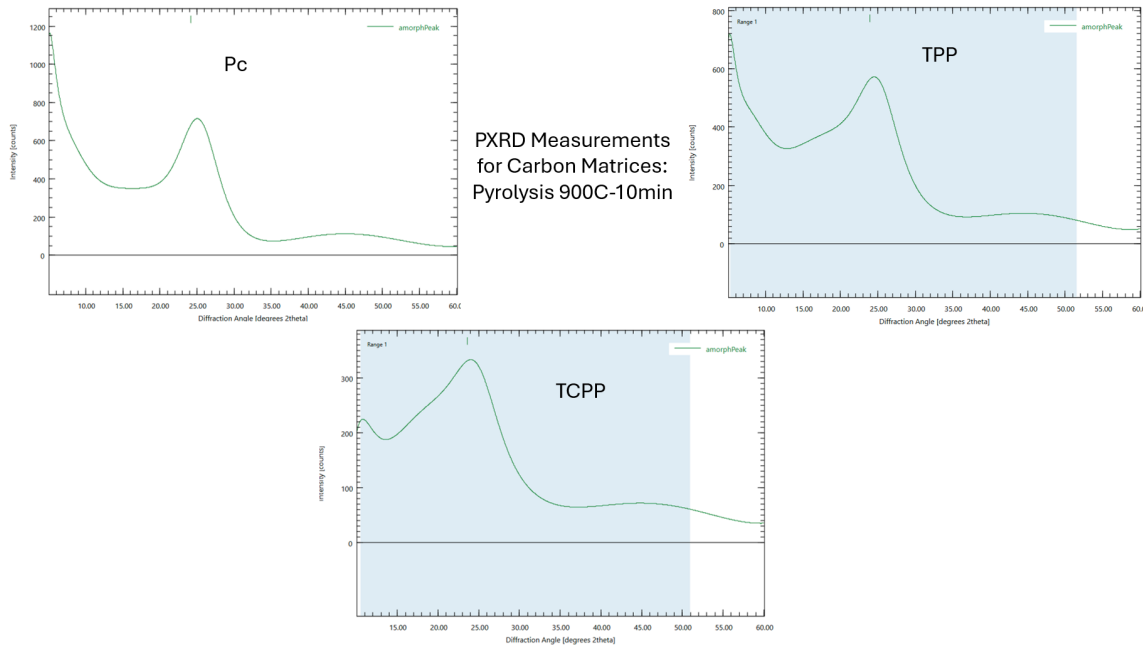
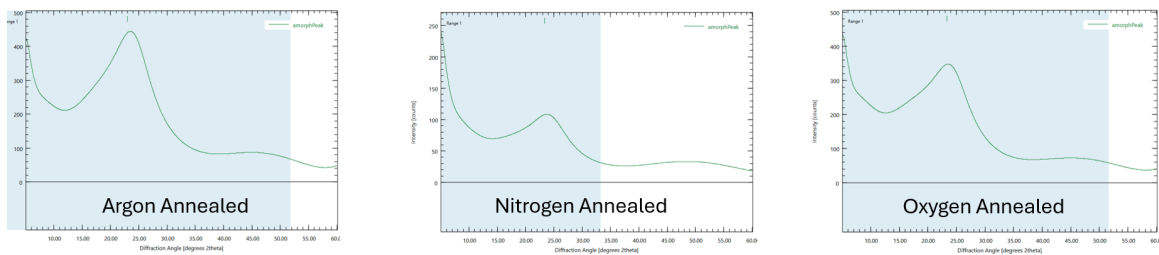


Figure 6.23: PXRD measurements for all carbon matrices: Pc, TCPP, and TPP.

They were pyrolyzed at 900C for 10min. Source: Vicente Pena Perez



PXRD Measurements for TCPP Matrices: Pyrolysis 900C-10min. Annealing: 150C-180min

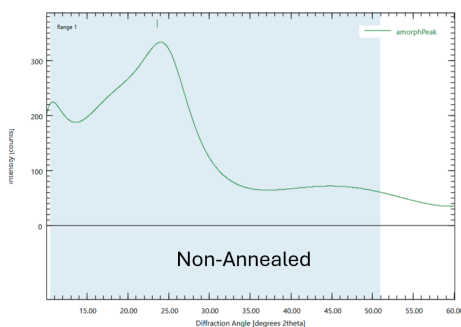


Figure 6.24: PXRD measurements for TCPP matrices. They were pyrolyzed at 900C for 10min. Also, annealed plots are shown. Source: Vicente Pena Perez

PXRD for FePc, FeTCPP, and FeTPP Nanoparticles

Our analysis through Powder X-ray Diffraction (PXRD) measurements has elucidated the complex phase behavior of carbon and iron in our nanoparticle samples, which vary significantly with pyrolysis conditions and annealing treatments. Figure 6.25 displays the presence of iron, iron alpha, graphite 2H, and graphite 3R phases in the FePc samples. As the temperature increases and the pyrolysis time extends, we observe an increase in counts, suggesting a reduction in amorphous material. In the case of FeTCPP, shown in Figure 6.26, the samples primarily exhibit phases of iron cementite and graphite 2H. At a pyrolysis duration of 180 minutes, we note the

highest count, indicative of phase partitioning. Following the 180-minute pyrolysis, annealing effects were investigated, revealing the appearance of iron austenite upon oxygen annealing, as depicted in Figure 6.27. Only measured at 180 minutes, the FeTPP samples (Figure 6.28) displayed phases of iron, iron alpha, iron austenite, and graphite 3R, illustrating the impact of different carbon matrices on the resultant phases in pyrolyzed precursors. Figure 6.29 compares all metal nanoparticles at a uniform pyrolysis temperature of 900 °C for 180 minutes, illustrating distinct phases of graphite and iron. We further analyzed the structural properties quantitatively. The optimal conditions, crystallinity percentages, and graphitization levels are summarized in Table 6.8, which also includes the average nanoparticle sizes. It is important to note that errors in these measurements are attributed to the complexities in fitting Gaussian profiles and the overlapping of phases in the samples. Our PXRD analyses provide comprehensive insights into the phase behavior and structural properties of iron and carbon in different nanoparticle matrices. The detailed qualitative and quantitative results underscore the complexity of the materials studied and the need for precise control over synthesis and processing conditions to tailor material properties effectively. The analysis showed that FeTCCP, pyrolyzed at 900 °C for 60 minutes and annealed in oxygen, exhibited the highest level of crystallinity at 81.86% with 28.74% graphitization. This sample had an interesting average nanoparticle diameter of 174.92 nm for iron cementite, indicating a high degree of structural ordering. Conversely, the FeTPP sample, processed under the same temperature but for

a duration of 180 minutes, was the least crystalline. Despite its high graphitization percentage of 95.66%, this sample displayed a complex distribution of nanoparticle sizes, with diameters of 17.54 nm for iron, 49.27 nm for iron alpha, and 1393.25 nm for iron austenite. These varied sizes and high graphitization suggest a significant transformation of the carbon matrix at extended pyrolysis durations. The PXRD analyses provide comprehensive insights into the phase behavior and structural properties of iron and carbon in different nanoparticle matrices. The detailed quantitative results underscore the complexity of the materials studied and highlight the need for precise control over synthesis and processing conditions to tailor material properties effectively. The noted discrepancies due to measurement complexities underscore the challenges inherent in characterizing such complex systems.

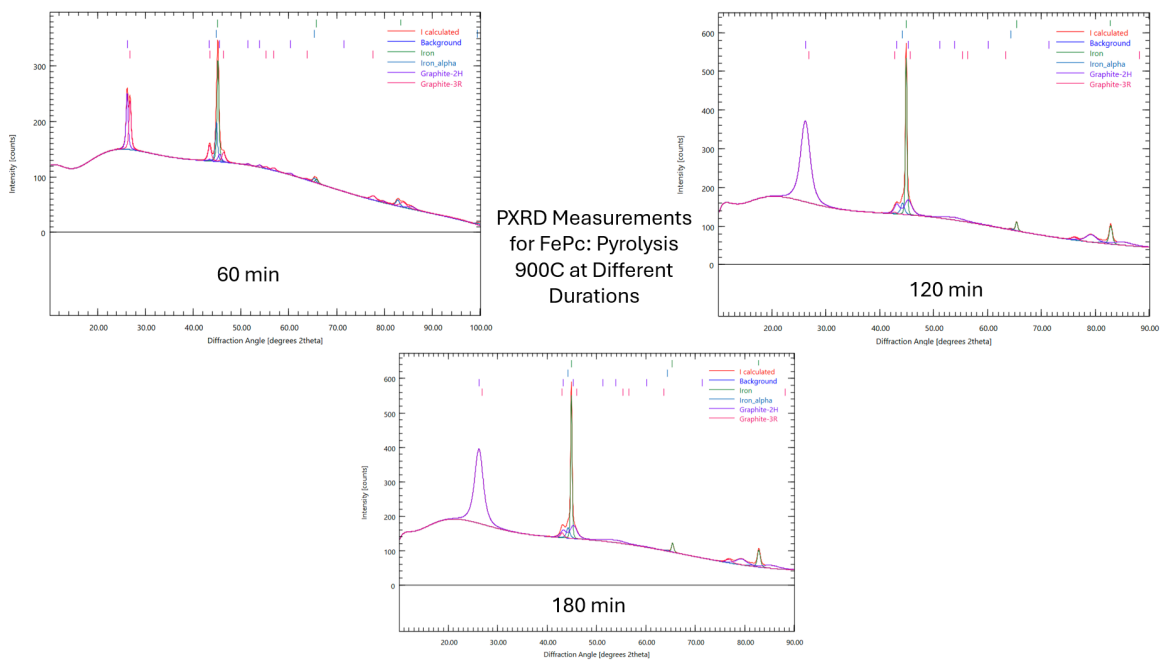


Figure 6.25: PXR measurements for FePc nanoparticles. They were pyrolyzed at 900C at different times. Source: Vicente Pena Perez

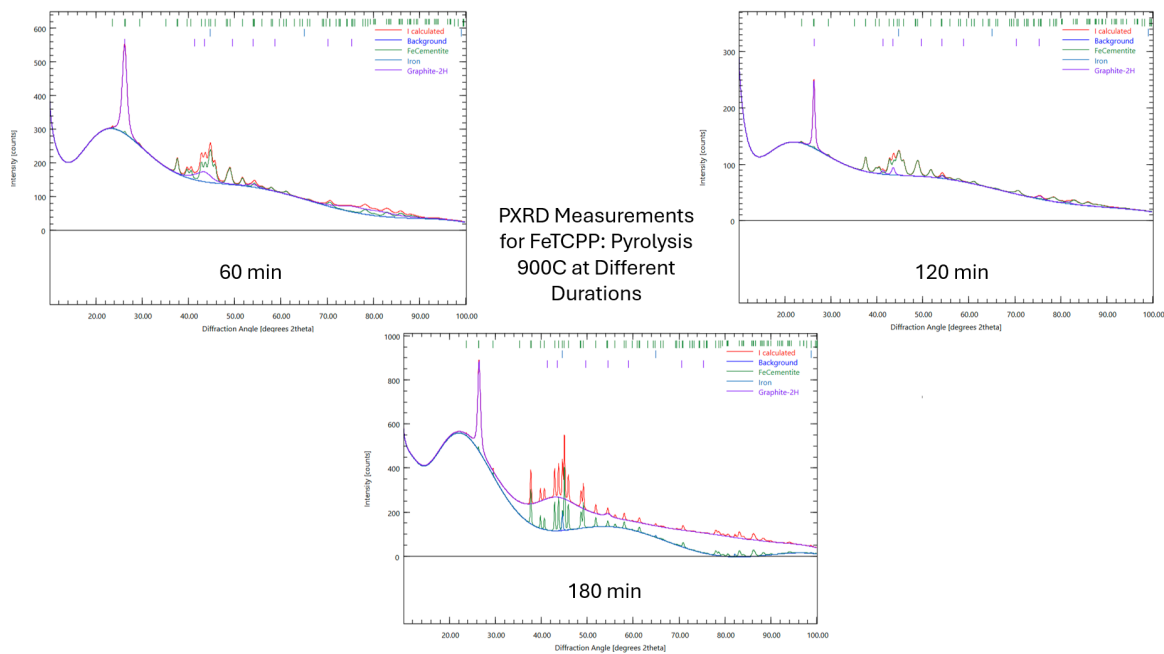


Figure 6.26: PXRD measurements for FeTCPP nanoparticles. They were pyrolyzed at 900C at different times. Source: Vicente Pena Perez

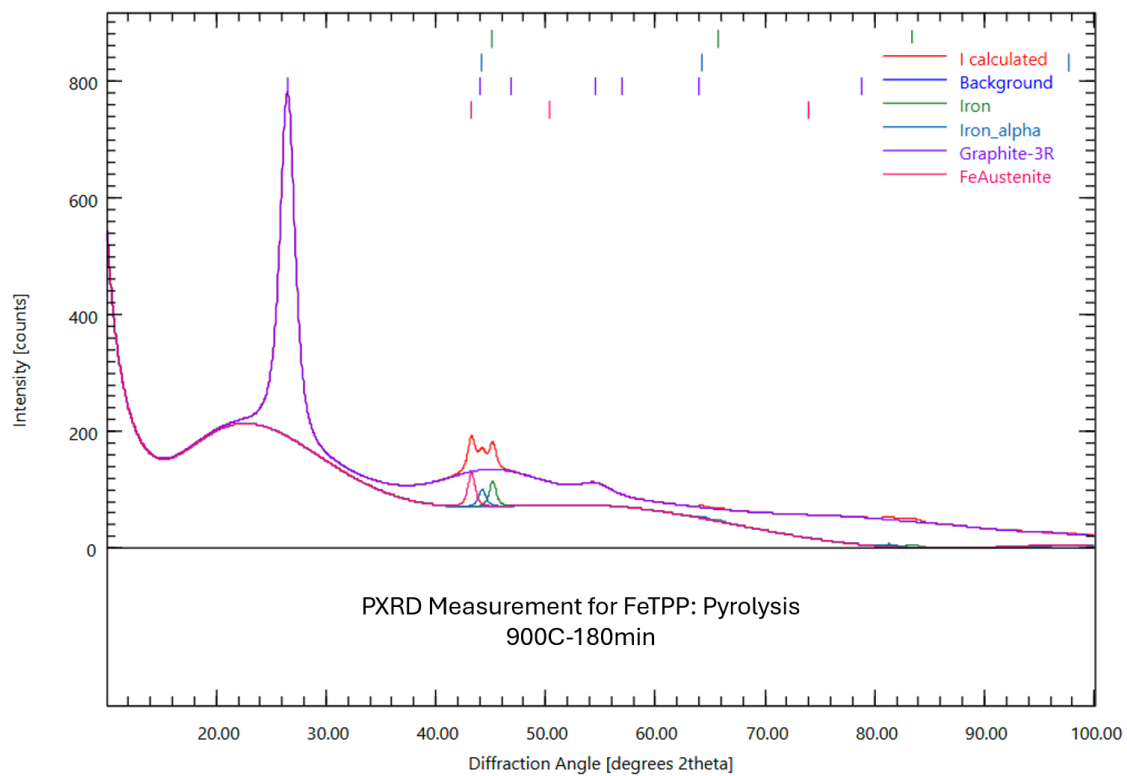


Figure 6.28: PXRD measurements for FeTPP nanoparticles. They were pyrolyzed at 900C for 180 minutes. Source: Vicente Pena Perez

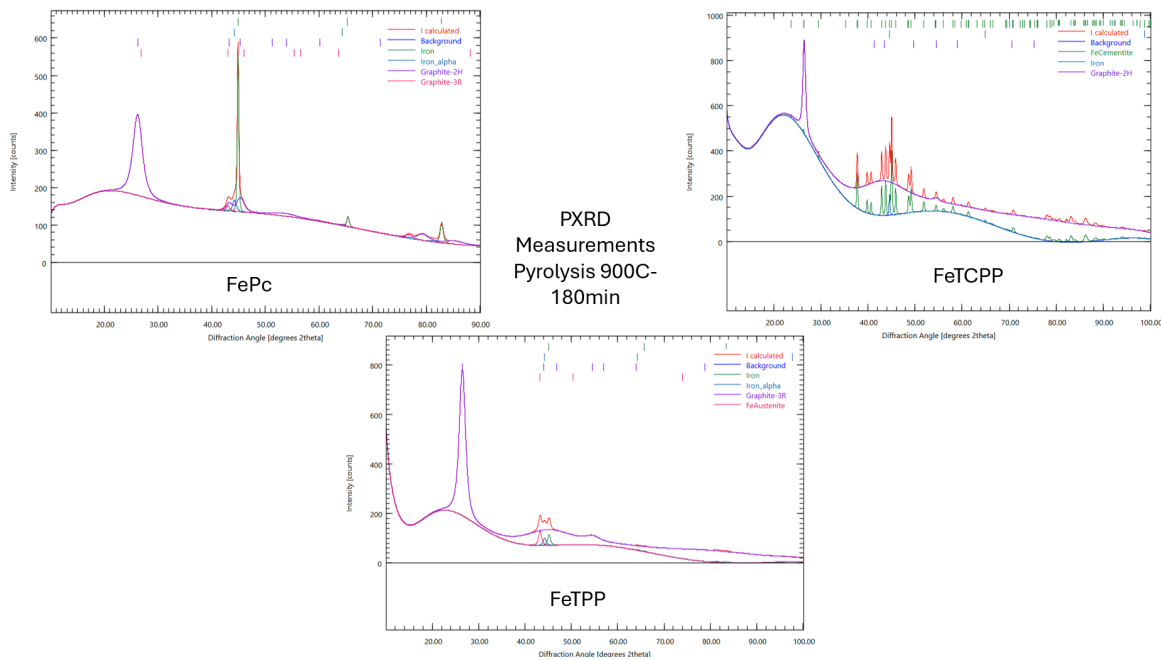


Figure 6.29: PXRD measurements for all nanoparticles. They were pyrolyzed at 900°C for 180 minutes. Source: Vicente Pena Perez

6.2.1 Size Characterization

Material 900C	Average Nanoparticle Sizes (nm)
FePc-60min	Graphite 2H: 28.63, Iron alpha: 53.25
FePc-120min	Graphite 2H: 232.36, Graphite 3R: 157.71, Iron: 108.65, Iron alpha: 47.54
FePc-180min	Graphite 2H: 27.061, Iron: 132.11, Iron alpha: 51.24
FeTCPP-60min	Graphite 2H: 70.96, Iron: 12.09, FeCementite: 75.55
FeTCPP-120min	Graphite 2H: 504.21, FeCementite: 34.044
FeTCPP-180min	Graphite 2H: 1091.023, Iron: 665.61, FeCementite: 1022.0093
FeTCPP-60min-Nitrogen	Graphite 2H: 5.96, Iron: 2822.96, FeCementite: 1029.56
FeTCPP-60min-Oxygen	Graphite 2H: 74.66, FeCementite: 174.92
FeTPP-180min	Graphite 3R: 14.84, Iron: 17.54, Iron Alpha: 49.27, FeAustenite: 1393.25

Table 6.8: Average nanoparticle sizes with pyrolysis at 900C

6.2.2 Crystallinity and Amorphous Regions

Material 900C	Lc (nm)	Graphitization Index (nm)	Crystallinity (%)	Graphitization (%)
FePc-60min	0.027	0.019	46.06	59.19
FePc-120min	0.054	0.038	30.82	75.60
FePc-180min	0.057	0.040	32.81	75.57
FeTCPP-60min	0.072	0.051	53.94	56.44
FeTCPP-120min	0.036	0.025	70.75	28.92
FeTCPP-180min	0.040	0.028	12.45	90.13
FeTCPP-60min Nitrogen	0.040	0.028	16.55	83.50
FeTCPP-60min Oxygen	0.036	0.025	81.86	28.74
FeTPP-180min	0.082	0.057	7.38	95.66

Table 6.9: Crystallinity and Amorphous Regions with pyrolysis at 900C

6.3 SEM and EDS Results

As part of our comprehensive analysis of carbon matrices and nanoparticle precursors, we utilized Scanning Electron Microscopy (SEM) and Energy Dispersive Spectroscopy (EDS) to examine the microstructural and elemental composition aspects of the samples. This section details the observations made and discusses the implications of these findings on the material properties and potential applications. The SEM images provided detailed visual insights into the morphology and surface characteristics of both the carbon matrices and the nanoparticle precursors. The high-resolution images allowed us to identify specific regions of interest where the structural integrity

and uniformity of particle distribution could be assessed. Measurements taken from the SEM images, such as particle size distribution and density areas, provide quantitative data that are essential for evaluating the synthesis quality and for tailoring the material properties to specific applications. EDS analysis was employed to determine the elemental composition of the samples. This technique was particularly useful in confirming the presence of desired elements and in detecting any impurities or variations in elemental distribution within the samples. The EDS results are crucial for understanding the chemical purity and the stoichiometric accuracy of the synthesized materials. Variations in elemental composition can significantly affect the physical and chemical properties of the nanoparticles, influencing their reactivity, stability, and suitability for specific applications. The combined SEM and EDS analyses have provided a deep insight into the microstructural and compositional characteristics of our samples. The results indicate that the synthesis processes used were largely successful in producing materials with desired properties and minimal impurities. However, the findings also highlight areas where improvements could be made, such as in controlling particle size distribution and enhancing elemental homogeneity. The SEM and EDS results conclude our exploration into the structural and elemental properties of carbon matrices and nanoparticle precursors. These analyses confirm the high quality of the materials synthesized and their potential for various applications. Moving forward, the insights gained from these results will guide the optimization of synthesis protocols and material processing techniques to further enhance the properties of

these nanoparticles.

SEM and EDS for Carbon Matrices

Figure 6.30 illustrates the morphological differences at scales of 10 μm for TCPP and TPP matrices, and 5 μm for the Pc matrix. The SEM images reveal a denser but smaller region of microspheres in Pc compared to TPP. Notably, TCPP shows almost no microspheres, indicating a distinct structural characteristic compared to the other two matrices. The differences in microsphere size and density across these matrices correlate with their magnetic responses observed in hysteresis loops. For TCPP and TPP, the absence or smaller radius of microspheres is associated with a better ferromagnetic response. In contrast, TPP with larger microsphere radii tends to exhibit a paramagnetic behavior with negligible ferromagnetic contribution in the hysteresis loops. EDS analysis was conducted to determine the elemental composition of the samples, with a particular focus on identifying any impurities or compositional variations that might affect their properties. The results, presented in Tables 6.10, 6.11, and 6.12, reveal the presence of predominantly carbon and traces of silicon, likely originating from the quartz tubes used during the pyrolysis process. The SEM and EDS analyses of the carbon matrices have provided valuable insights into the microstructural differences and their impact on the magnetic properties of the materials. The findings underscore the importance of microstructural control in optimizing the magnetic responses of carbon-based materials, offering guidance for future material design and synthesis strategies.

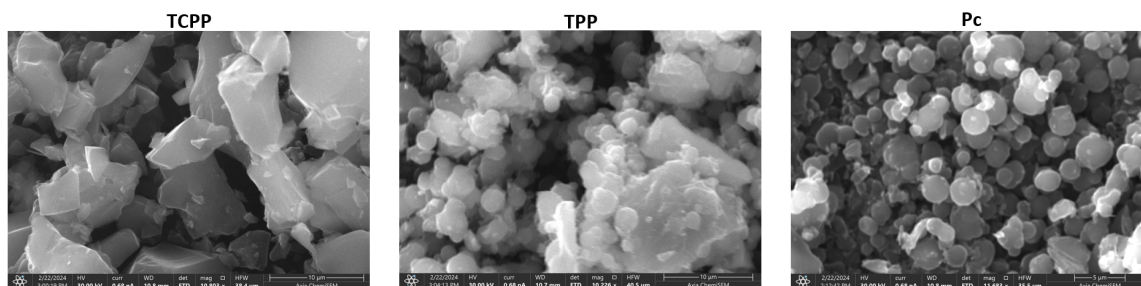


Figure 6.30: SEM images for the carbon matrices: TCPP is shown at a magnification of 10,803 times its size, with a accelerating voltaje of 30kV, and scale bar of 10 micrometers. TPP is shown at a magnification of 10,226 times its size, with a accelerating voltaje of 30kV, and scale bar of 10 micrometers. Pc is shown at a magnification of 11,683 times its size, with a accelerating voltaje of 30kV, and scale bar of 5 micrometers. Source: Vicente Pena Perez

Element	Atomic %	Atomic % Error	Weight %	Weight % Error	Net Counts
C	98.9	0.4	97.4	0.4	477,954
Si	1.1	0.0	2.5	0.0	41,170

Table 6.10: Elemental composition of the TCPP matrix with Pyrolysis at 900C-10min

Element	Atomic %	Atomic % Error	Weight %	Weight % Error	Net Counts
C	99.0	0.4	97.5	0.4	944,898
Si	0.6	0.0	1.4	0.0	41,154

Table 6.11: Elemental composition of the TPP matrix with Pyrolysis at 900C-10min

Element	Atomic %	Atomic % Error	Weight %	Weight % Error	Net Counts
C	99.8	0.4	99.5	0.4	3,232,489
Si	0.1	0.0	0.3	0.0	23,891

Table 6.12: Elemental composition of the Pc matrix with Pyrolysis at 900C-10min

SEM and EDS Analysis for Mixed Carbon Matrices

Figure 6.31 displays SEM images at various scales, 1 μm for the mixture of 75% TCPP and 25% TPP matrices, 5 μm for the mixture of 50% TCPP and 50% TPP matrices, and 2 μm for the the mixture of 25% TCPP and 75% TPP. These images reveal a progression from less dense semi-microspheres in higher TCPP proportions to more dense quasi-microspheres and finally to denser microspheres within larger carbon structures in the mixture with a higher TPP content. The greatest density is observed in the 25% TCPP and 75% TPP mixture, which corresponds to the most stable blended matrix configuration. EDS analysis was conducted to assess the elemental composition of these mixed matrices. The presence of predominantly carbon along with traces of silicon, nitrogen, and oxygen is consistent across the samples. The results, presented in Tables 6.13, 6.14, and 6.15, reveal the presence of predominantly carbon and traces of silicon, nitrogen and oxygen, likely originating from the quartz tubes used during the pyrolysis process. The detected nitrogen and oxygen indicate that the pyrolysis duration was not sufficient to eliminate all vacancies and allow for the complete escape of oxygen from the matrix, which is beneficial as it enhances matrix stability. The SEM and EDS analyses of mixed carbon matrices have

underscored the importance of microstructural control in optimizing the magnetic responses of carbon-based materials. These insights are invaluable for guiding future material design and synthesis strategies, particularly in applications where magnetic properties are critical.

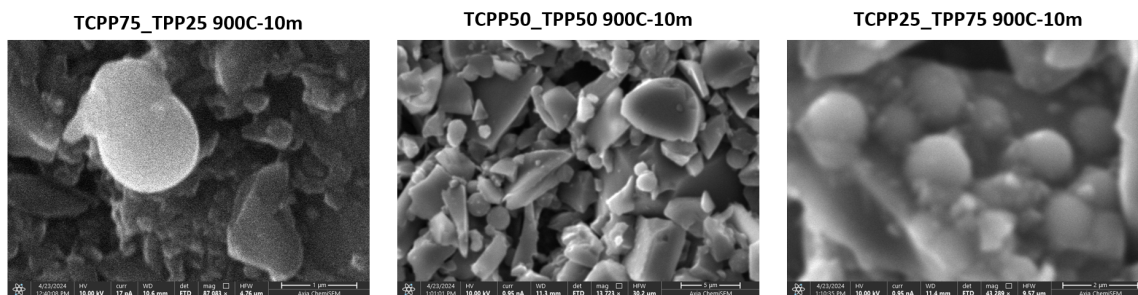


Figure 6.31: SEM images for the mixed carbon matrices: The first is shown at a magnification of 87,083 times its size, with a accelerating voltage of 10kV, and scale bar of 1 micrometers. Second is shown at a magnification of 13,723 times its size, with a accelerating voltage of 10kV, and scale bar of 5 micrometers. Third is shown at a magnification of 43,289 times its size, with a accelerating voltage of 10kV, and scale bar of 2 micrometers. Source: Vicente Pena Perez

Element	Atomic %	Atomic % Error	Weight %	Weight % Error	Net Counts
C	94.8	1.5	93.1	1.4	2,137
O	5.2	1.4	6.9	1.8	27

Table 6.13: Elemental composition of the 50% TCPP with 50% TPP matrix with Pyrolysis at 900C-10min

Element	Atomic %	Atomic % Error	Weight %	Weight % Error	Net Counts
C	76.0	0.3	69.9	0.3	271,139
N	8.7	0.4	9.3	0.4	6,838
O	13.0	0.2	15.9	0.3	16,333
Si	2.3	0.0	4.9	0.1	13,095

Table 6.14: Elemental composition of the 25% TCPP with 75% TPP matrix with Pyrolysis at 900C-10min

Element	Atomic %	Atomic % Error	Weight %	Weight % Error	Net Counts
C	98.9	0.4	97.6	0.4	495,905
Si	1.1	0.0	2.4	0.0	6,890

Table 6.15: Elemental composition of the 75% TCPP with 25% TPP matrix with Pyrolysis at 900C-10min

SEM and EDS for Nanoparticles FePc, FeTCPP, and FeTPP

Figure 6.32 presents two SEM images for the FePc nanoparticles. The left image shows a 5 μm region, illustrating a high concentration of iron, carbon, and silicon, corroborated by the elemental analysis in Table 6.16. The right image highlights a microsphere with a clear morphology and surface defects, measuring about 2 μm in radius, a feature uncommon in metal-based systems. In contrast, Figure 6.33 shows SEM images of FeTCPP and FeTPP, both covering 20 μm regions. These images reveal that FeTPP has a less dense region compared to FeTCPP. This observation aligns with the results from the elemental analyses in Tables 6.17 and 6.18, where iron content is higher in FeTPP and carbon density is greater in FeTCPP, suggesting

variations in particle aggregation and elemental distribution. The SEM and EDS analyses for FePc, FeTCPP, and FeTPP nanoparticles have provided significant insights into their microstructural and elemental properties. These analyses have revealed crucial differences in density, particle aggregation, and elemental distribution among the nanoparticle types studied. The observations are particularly valuable for understanding the physical and chemical environments within each type of nanoparticle and how these environments may influence their functional properties. The presence of unexpected microspheres in FePc and the variations in density and elemental composition between FeTCPP and FeTPP highlight the influence of synthesis conditions on nanoparticle formation. These findings suggest that the microstructural characteristics directly impact the magnetic responses and stability of the nanoparticles, which is critical for applications ranging from catalysis to magnetic data storage. Based on the SEM and EDS results, further research is recommended to optimize synthesis protocols to enhance uniformity and purity in nanoparticle production. Adjusting factors such as temperature, duration, and atmospheric conditions during synthesis could lead to improved control over particle morphology and elemental composition.

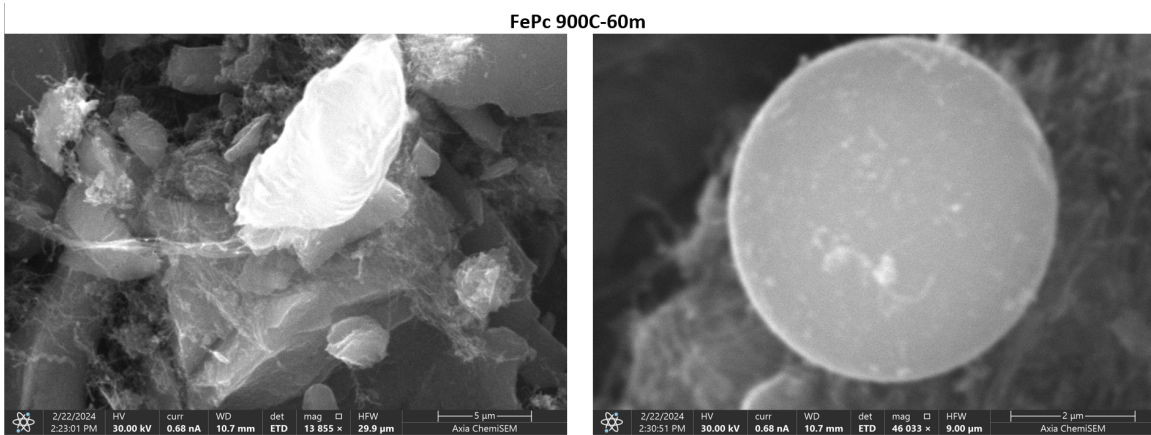


Figure 6.32: SEM images for FePc: The first is shown at a magnification of 13,855 times its size, with a accelerating voltage of 30kV, and scale bar of 5 micrometers. It shows an overall region of interest for EDS. Second is shown at a magnification of 46,033 times its size, with a accelerating voltage of 30kV, and scale bar of 2 micrometers. This image shows a micro-sphere. Source: Vicente Pena Perez

Element	Atomic %	Atomic % Error	Weight %	Weight % Error	Net Counts
C	96.6	0.4	86.3	0.4	1,147,482
Fe	3.2	0.0	13.3	0.0	345,302
Si	0.1	0.0	0.1	0.0	6,095

Table 6.16: Elemental composition of the FePc 900C-60min

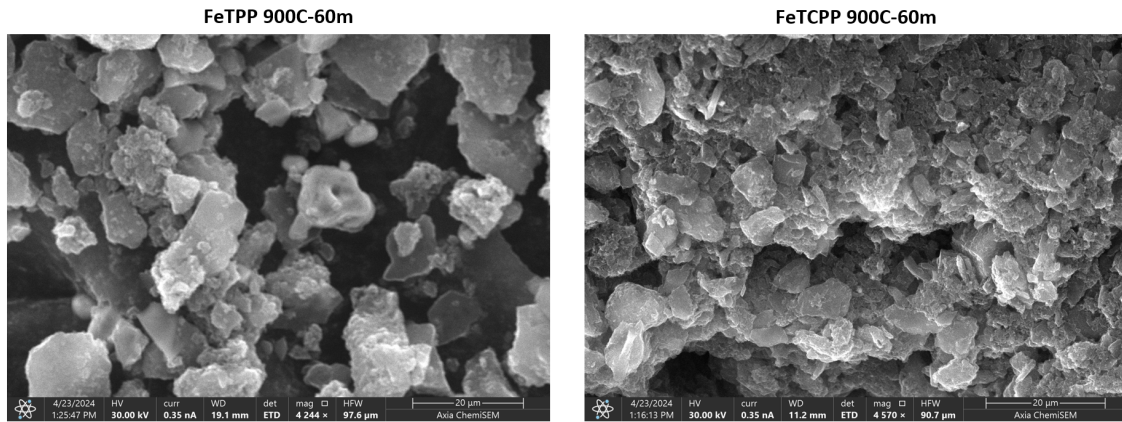


Figure 6.33: SEM images for FeTCPP and FeTPP: The first is shown at a magnification of 4,244 times its size, with a accelerating voltage of 30kV, and scale bar of 20 micrometers. Second is shown at a magnification of 4,570 times its size, with a accelerating voltage of 30kV, and scale bar of 20 micrometers. Source: Vicente Pena Perez

Element	Atomic %	Atomic % Error	Weight %	Weight % Error	Net Counts
C	80.2	0.4	70.4	0.3	407,189
Fe	2.0	0.0	8.2	0.1	87,067
Si	0.5	0.0	1.0	0.0	19,750

Table 6.17: Elemental composition of the FeTPP 900C-60min

Element	Atomic %	Atomic % Error	Weight %	Weight % Error	Net Counts
C	98.1	0.4	92.0	0.4	965,505
Fe	1.7	0.0	7.5	0.0	130,812
Si	0.1	0.0	0.2	0.0	5,940

Table 6.18: Elemental composition of the FeTCPP 900C-60min

6.4 TEM & Algorithm Results

Our initial analysis begins with a sample of Iron(II) Phthalocyanine (FePc) pyrolyzed at 250 degrees Celsius for 180 minutes. Using HRSTEM imagery within the 20nm range, our algorithm was employed to identify and count junction types. Subsequently, focusing on a different area of the same sample, specifically in the 50nm range, we detected nanostructures that appeared to be elliptical in shape. The procedure was replicated for the same sample set but viewed at a different angle to ensure consistency of the analysis.

Histograms for the areas, eccentricities, perimeters, and major axes lengths were generated and are presented below. The porosity of the samples was also calculated and is discussed. This same process was then repeated for samples of Iron(II) Porphyrin (FePr), albeit under different initial conditions—specifically, 150 degrees Celsius for the pyrolysis duration of 30 minutes.

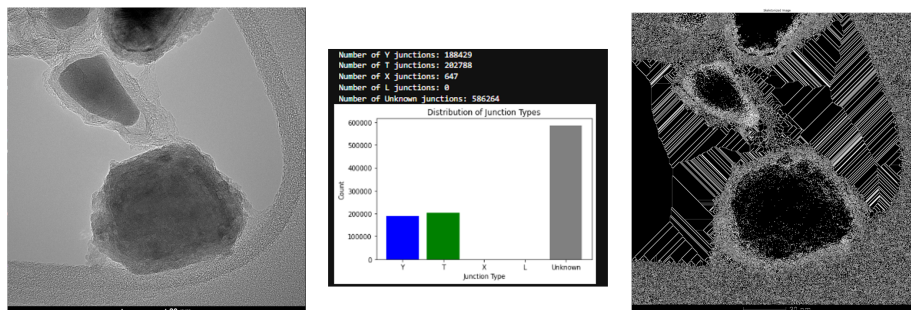


Figure 6.34: Going from left to right: HRSTEM image showing the morphology of the sample at 20nm scale, graphical representation of junction types and counts derived from the algorithm, and skeletonized image of the sample highlighting the detected junctions.

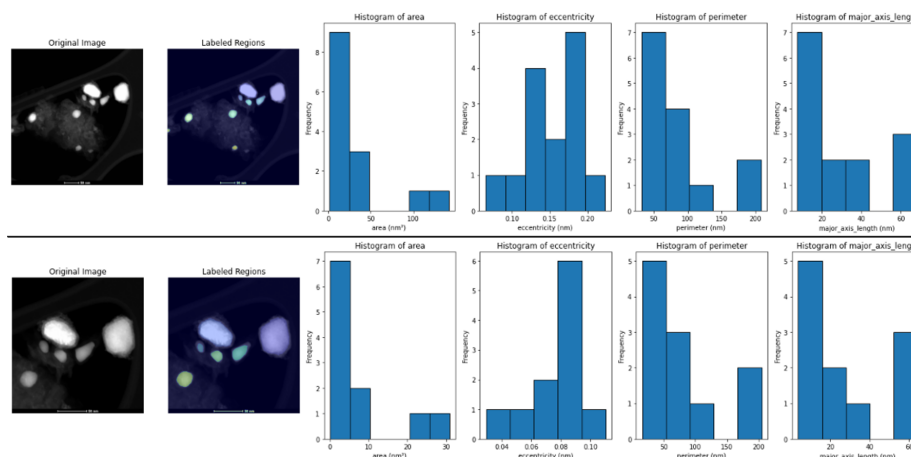


Figure 6.35: Size characterization of FePc samples with histograms of area, eccentricity, perimeter, and major axis length. For the first field of view, the areas range from 50 to 150 nm^2 , and the length of the major axes from 20 to 75 nm. For the second field of view, we get areas from 5 to 35 nm^2 and length of major axes from 20 to 75nm. Source of first HRSTEM image: Penn State

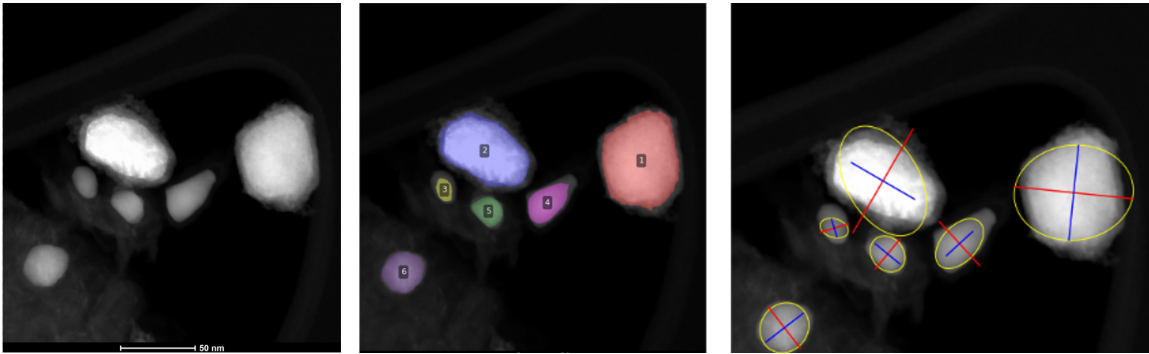


Figure 6.36: Labeled regions of FePc samples indicating the size and shape of nanostructures. The first image on the left is the original 50nm range field of view. The second image is the detected nanostructures by the algorithm. Third image is the shape detected over the original image with yellow denoting the perimeter, red the major axes, and blue the minor axes.

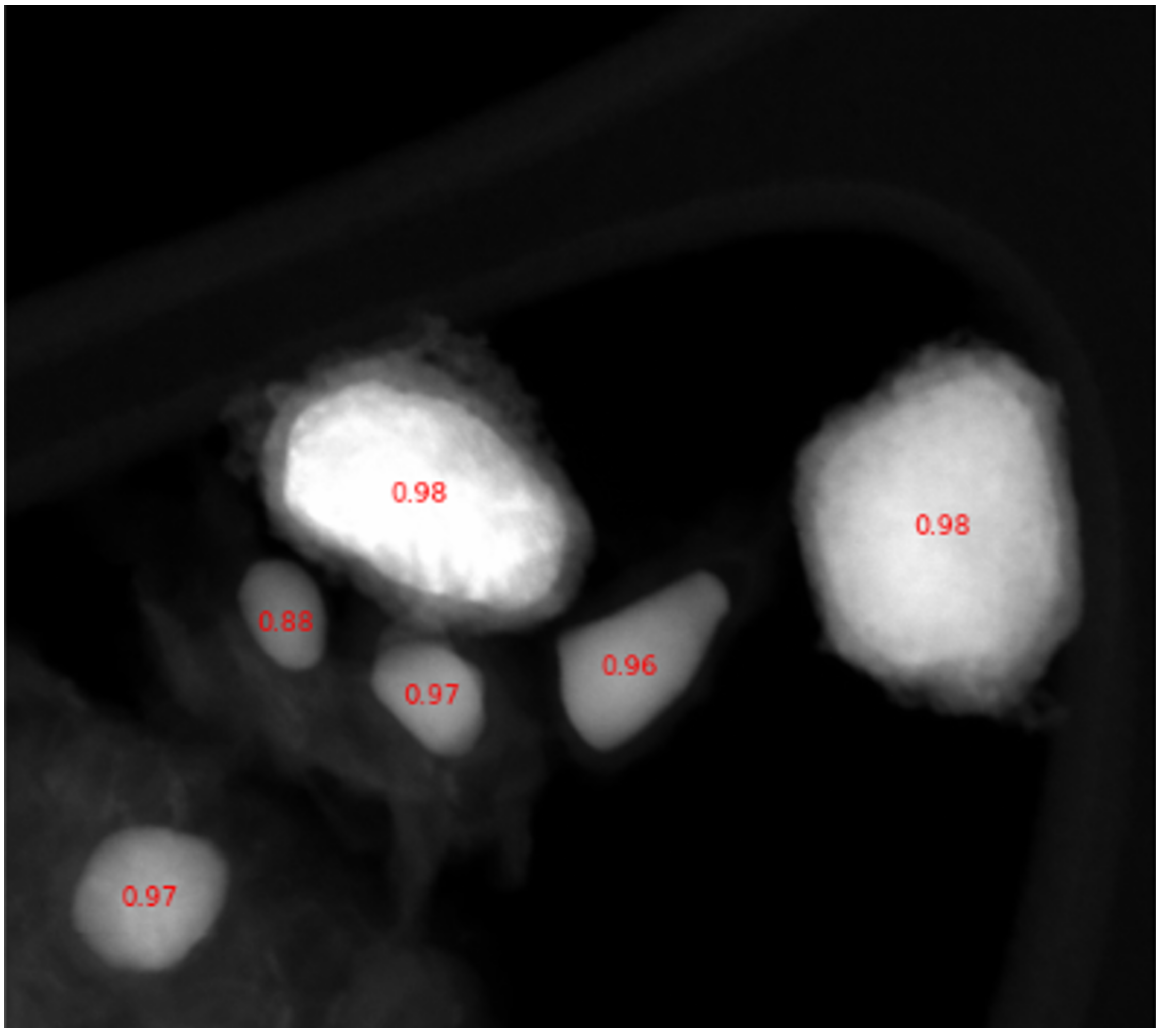


Figure 6.37: Porosity characterization of FePc samples with individual pore measurements. Note that the degree of porosity detected by the algorithm is high, meaning that there is mostly material, and less empty space.

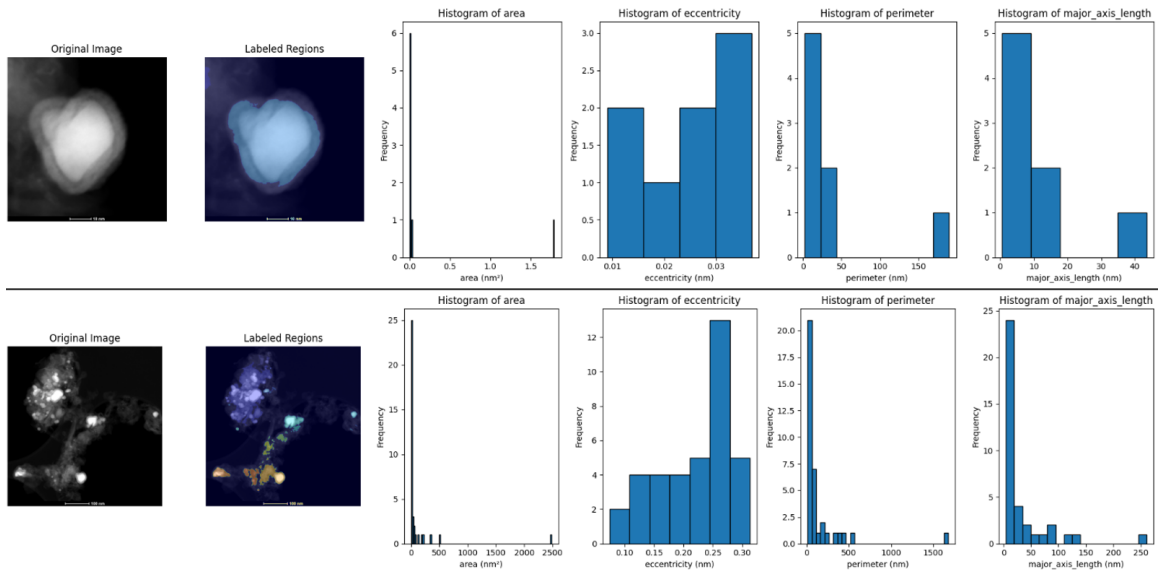


Figure 6.38: Comparative size characterization for FePr samples with histograms of area, eccentricity, perimeter, and major axis length. For the first field of view, the areas range from 0.5 to 2.5 nm^2 , and the length of the major axes from 10 to 50 nm. For the second field of view, we get areas from 100 to 2500 nm^2 and length of major axes from 10 to 250nm.

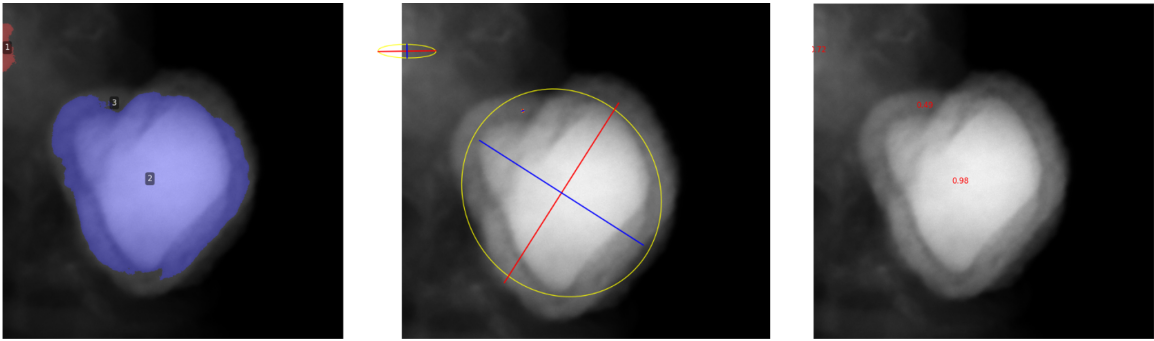


Figure 6.39: Labeled regions of FePr samples showcasing the distribution of nanostructures, as well as porosity. The first image on the left is the original with the detected nanostructure in color. The second image is the shape detected over the original image with yellow denoting the perimeter, red the major axes, and blue the minor axes. The third image is the porosity.

CHAPTER 7

Discussion

This study has provided a foundational exploration into the complexities of carbon-based nanoparticles, particularly focusing on the magnetic properties and structural characteristics of Pc, TCPP, and TPP matrices. By conducting extensive experiments under varying pyrolysis temperatures and durations and utilizing different annealing atmospheres—namely Argon, Nitrogen, and Oxygen—we have identified Nitrogen and Oxygen as particularly effective in stabilizing the more robust matrices of Pc and TCPP. This research underscores the need for further exploration into optimal annealing times and pyrolysis conditions, potentially extending the duration from 60 to 180 minutes to better understand the effects on graphitization and crystallinity.

The magnetic properties of these materials were rigorously analyzed through hysteresis loops at VSM temperatures ranging from 5K to 300K. These studies were enhanced by a custom-developed algorithm, refined through collaborative feedback within the research group, which aided significantly in data interpretation and analysis.

Further extending our research to iron-added matrices such as FePc, FeTCPP, and FeTPP, we discovered that FeTCPP exhibited the most promising properties under varied experimental conditions. By systematically studying the impact of ex-

tended pyrolysis durations (from 60 to 180 minutes) and analyzing PPMS measurements at 300K and 10K, we identified critical magnetic parameters such as saturation, remanence, and coercivity. The ratio M_r/M_s , critical for applications in hyperthermia treatment, indicated potential maxima that warrant further exploration to determine their global or local nature. Comparative studies with other metal nanoparticles like CuTPP, CoTPP, and NiTPP suggested that optimal pyrolysis might be achieved at 900°C for 60 minutes.

Moreover, PXRD analyses facilitated by another component of our proprietary algorithm revealed essential metrics such as average nanoparticle size, phase identification, crystallite size, graphitization index, and crystallinity percentages. These measurements provided a granular view of the nanoparticles' structural attributes, essential for tailoring materials to specific applications.

The in-depth SEM and EDS analyses contributed significantly to understanding the microstructural and elemental details of FePc, FeTCPP, and FeTPP nanoparticles. These findings are crucial for refining synthesis strategies and ensuring the reproducibility and efficacy of nanoparticles, particularly in medical applications like cancer treatment.

This integrated methodological approach has not only advanced our understanding of magnetic nanostructures but also established a robust framework for future investigations. While the current findings are promising, they represent initial steps in a broader research trajectory. Ongoing and future studies will focus on

varying pyrolysis conditions and expanding the scope to include different metal centers within porphyrin and phthalocyanine structures. Additionally, translating these laboratory-scale discoveries into clinical applications, particularly for cancer therapy, remains a primary goal. This endeavor will involve further HRSTEM measurements and continuous refinement of our analytical algorithms to ensure the comprehensive characterization and effective application of these novel materials.

REFERENCES

- [Arrhenius, 1889] Arrhenius, S. (1889). Über die reaktionsgeschwindigkeit bei der inversion von rohrzucker durch säuren. *Zeitschrift für Physikalische Chemie*, 4:226–248.
- [Avrami, 1939] Avrami, M. (1939). Kinetics of phase change. i general theory. *Journal of Chemical Physics*, 7:1103–1112.
- [Barrett et al., 1951] Barrett, E. P., Joyner, L. G., and Halenda, P. P. (1951). The determination of pore volume and area distributions in porous substances. i. computations from nitrogen isotherms. *Journal of the American Chemical Society*, 73(1):373–380.
- [Brunauer et al., 1938] Brunauer, S., Emmett, P. H., and Teller, E. (1938). Adsorption of gases in multimolecular layers. *Journal of the American Chemical society*, 60(2):309–319.
- [Chen et al., 2020] Chen, K., Liu, K., An, P., Li, H., Lin, Y., Hu, J., Jia, C., Fu, J., Li, H., Liu, H., and et al. (2020). Iron phthalocyanine with coordination induced electronic localization to boost oxygen reduction reaction.
- [Chilukuri et al., 2020] Chilukuri, B., Mazur, U., and Hipps, K. W. (2020). Structure, properties, and reactivity of porphyrins on surfaces and nanostructures with periodic dft calculations. *Applied Sciences*, 10(3).

- [Horvath and Kawazoe, 1983] Horvath, G. and Kawazoe, K. (1983). Method for the calculation of effective pore size distribution in molecular sieve carbon. *Journal of Chemical Engineering of Japan*, 16(6):470–475.
- [Inamura et al., 2019] Inamura, I., Inamura, K., Jinbo, Y., Mihara, T., and Sasaoka, Y. (2019). Preparation of metal phthalocyanine (mpc)–polymer complexes: the possible anti-cancer properties of fepc–polymer complexes. *Heliyon*, 5.
- [Joubert et al., 2023] Joubert, J. C., Wilke, D. N., and Pizette, P. (2023). Fourier Image Analysis of Multiphase Interfaces to Quantify Primary Atomization. *Mathematical and Computational Applications*, 28(2):55.
- [Kissinger, 1957] Kissinger, H. (1957). Reaction kinetics in differential thermal analysis. *Analytical Chemistry*, 29(11):1702–1706.
- [Kocharian et al.,] Kocharian, A., Iglesias, F., Alvarado, C., Khodagulyan, A., Bernal, O., Shallenberger, J., and Wonderling, N. Syntheses, magnetic and structural properties of core-shell fepc and fepr nanoparticles annealed by oxygen and nitrogen at different temperatures.
- [Koshino and Ando, 2008] Koshino, M. and Ando, T. (2008). Diamagnetic response of graphene multilayers. *Physica E: Low-dimensional Systems and Nanostructures*, 40(5):1014–1016.
- [Langmuir, 1918] Langmuir, I. (1918). The adsorption of gases on plane surfaces of glass, mica and platinum. *Journal of the American Chemical Society*, 40(9):1361–

1403.

- [Le Pouliquen et al., 2005] Le Pouliquen, F., Da Costa, J.-P., Germain, C., and Baylou, P. (2005). A new adaptive framework for unbiased orientation estimation in textured images. *Pattern Recognition*, 38(11):2032–2046.
- [Lifshitz and Slyozov, 1961] Lifshitz, I. M. and Slyozov, V. V. (1961). The kinetics of precipitation from supersaturated solid solutions. *Journal of Physics and Chemistry of Solids*, 19(1-2):35–50.
- [Lin et al., 2017] Lin, F., Zhu, Z., Zhou, X., Qiu, W., Niu, C., Hu, J., Dahal, K., Wang, Y., Zhao, Z., Ren, Z., Litvinov, D., Liu, Z., Wang, Z. M., and Bao, J. (2017). Orientation Control of Graphene Flakes by Magnetic Field: Broad Device Applications of Macroscopically Aligned Graphene. *Advanced Materials*, 29(1):1604453.
- [Neamtu et al., 2020] Neamtu, M., Nadejde, C., Brinza, L., Dragos, O., Gherghel, D., and Paul, A. (2020). Iron phthalocyanine-sensitized magnetic catalysts for BPA photodegradation. *Scientific Reports*, 10(1):5376.
- [Nelson et al.,] Nelson, F. A., Louis, H., Benjamin, I., and A. Timothy, R. The iron group transition-metal (Fe, Ru, Os) coordination of Se-doped graphitic carbon (Se@g-C₃N₄) nanostructures for the smart therapeutic delivery of zidovudine (ZVD) as an antiretroviral drug: a theoretical calculation perspective. *RSC Advances*, 13(48):34078–34096.
- [Potter et al., 2019] Potter, M. E., Riley, L. N., Oakley, A. E., Mhembere, P. M.,

- Callison, J., and Raja, R. (2019). The influence of porosity on nanoparticle formation in hierarchical aluminophosphates. *Beilstein Journal of Nanotechnology*, 10:1952–1957.
- [Pré et al., 2013] Pré, P., Huchet, G., Jeulin, D., Rouzaud, J.-N., Sennour, M., and Thorel, A. (2013). A new approach to characterize the nanostructure of activated carbons from mathematical morphology applied to high resolution transmission electron microscopy images. *Carbon*, 52:239–258.
- [Sharma et al., 1999] Sharma, A., Kyotani, T., and Tomita, A. (1999). A new quantitative approach for microstructural analysis of coal char using hrtem images. *Fuel*, 78(10):1203–1212.
- [Shim et al., 2000] Shim, H.-S., Hurt, R. H., and Yang, N. Y. (2000). A methodology for analysis of 002 lattice fringe images and its application to combustion-derived carbons. *Carbon*, 38(1):29–45.
- [Stephenson and Bell, 2007] Stephenson, N. A. and Bell, A. T. (2007). Mechanistic insights into iron porphyrin-catalyzed olefin epoxidation by hydrogen peroxide: Factors controlling activity and selectivity. *Journal of Molecular Catalysis A: Chemical*, 275(1):54–62.
- [Yang et al., 2022] Yang, H., Yang, Y., Yin, Y., Wang, Y., Shang, Y., Jin, L., Li, Y., and Hu, H. (2022). Modeling char surface area during coal pyrolysis: Validation of relationship between pore structure and polymer network. *AIChE Journal*, 68(8):e17723.

[Zhou et al., 2024] Zhou, W., Ding, J., Hua, J., Zhang, L., Watanabe, K., Taniguchi, T., Zhu, W., and Xu, S. (2024). Layer-polarized ferromagnetism in rhombohedral multilayer graphene. *Nature Communications*, 15(1):2597.

APPENDIX A

Nanoparticle Analyzer

A.1 Libraries

Important libraries used in the python script.

```
1 import numpy as np
2 from skimage import io, filters, morphology, measure, color, feature
3 from scipy.fftpack import fft2, fftshift, ifft2, ifftshift
4 from skimage.morphology import skeletonize
5 from skimage.measure import label, regionprops
6 import numpy as np
7 import matplotlib.pyplot as plt
8 import os
9 import hyperspy.api as hs
10 import matplotlib.patches as mpatches
11 from skimage.filters import threshold_otsu
```

A.2 Structure Finding Part

```
1     def skeletonize_and_isolate_nodes(filtered_image,
2     node_threshold_factor):
3     """
4     Skeletonize the filtered image and isolate nodes by increasing
5     the threshold.
```

```

4     """
5     # Skeletonize
6     thresh = filters.threshold_otsu(filtered_image)
7     binary_image = filtered_image > thresh
8     skeleton = skeletonize(binary_image)
9
10    # Isolate nodes
11    nodes_thresh = thresh * node_threshold_factor
12    nodes_only = binary_image & (filtered_image > nodes_thresh)
13
14    return skeleton, nodes_only
15
16 def find_junctions(skeleton):
17     # Label the skeletonized image to identify distinct lines
18     labeled_skeleton = label(skeleton)
19     props = regionprops(labeled_skeleton)
20
21     junctions = np.zeros_like(skeleton)
22
23     # Detect crystal structures
24     crystal_structures = {'hematite': generate_crystal_template('
hematite'),
25                           'magnetite': generate_crystal_template('
magnetite'),
26                           'maghemite': generate_crystal_template('

```

```

maghemite'})}
27
28     for prop in props:
29         if prop.area > 1: # Ignore single pixel lines
30             coords = prop.coords
31             for y, x in coords:
32                 # Ensure that we don't go out of bounds
33                 if y > 0 and y < skeleton.shape[0] - 1 and x > 0 and
x < skeleton.shape[1] - 1:
34                     if skeleton[y, x] and np.sum(skeleton[y-1:y+2, x
-1:x+2]) > 3:
35                         junctions[y, x] = 1 # Mark junction points
36
37                 # Detect crystal structures and mark their
junctions
38                 for crystal, pattern in crystal_structures.items
():
39                     if pattern.shape[0] > 3 or pattern.shape[1]
> 3:
40                         continue
41                     if pattern_match(skeleton[y-1:y+2, x-1:x+2],
pattern):
42                         junctions[y, x] = 1 # Mark as a
junction due to crystal structure match
43     return junctions

```

```

44
45 def categorize_junctions(junctions, skeleton):
46     categorized_junctions = {'Y': [], 'T': [], 'X': [], 'L': [], '
Unknown': [],
47                               'Hematite': [], 'Magnetite': [], '
Maghemite': []}
48
49     for (y, x), value in np.ndenumerate(junctions):
50         if value:
51             junction_type = categorize_junction(y, x, skeleton)
52
53             # Check if this junction is also a crystal structure
junction
54             if junctions[y, x] == 1 and
is_crystal_structure_junction((y, x), skeleton):
55                 categorized_junctions[junction_type].append((y, x))
56             else:
57                 categorized_junctions['Unknown'].append((y, x))
58
59     return categorized_junctions

```

A.3 Feature Enhancement Part

```

1     def process_hrtem_image(image_path):
2         """
3         Process an HRTEM image to filter, skeletonize, reconnect fringes

```

```

, identify link types,
4   and detect specific crystal structures (hematite, magnetite,
maghemite).
5   """
6   # Load the image and check if it's loaded correctly
7   hrtem_image = io.imread(image_path, as_gray=True)
8   if hrtem_image.size == 0:
9       raise ValueError(f"Image at {image_path} could not be loaded
or is empty.")
10
11  # Apply step filter and skeletonize
12  filtered_image = apply_step_filter(hrtem_image, radius=1250)
13  if filtered_image.size == 0:
14      raise ValueError("Filtered image is empty.")
15
16  skeleton, nodes_only = skeletonize_and_isolate_nodes(
filtered_image, node_threshold_factor=1.5)
17  if skeleton.size == 0:
18      raise ValueError("Skeletonized image is empty.")
19
20  # Reconnect fringes
21  reconnected_skeleton = reconnect_fringes(skeleton)
22  if reconnected_skeleton.size == 0:
23      raise ValueError("Reconnected skeleton is empty.")
24

```

```

25     # Find and categorize junctions including new crystal structure
matches
26     junctions = find_junctions(reconnected_skeleton)
27     categorized_junctions = categorize_junctions(junctions,
reconnected_skeleton)
28
29     # Detect specific crystal structures
30     crystal_structures = ['hematite', 'magnetite', 'maghemite']
31     for crystal in crystal_structures:
32         pattern = generate_crystal_template(crystal)
33         matches = pattern_match(reconnected_skeleton, pattern)
34         categorized_junctions[crystal] = matches
35
36     return categorized_junctions, filtered_image,
reconnected_skeleton, junctions
37
38 def process_tem_image(image_path, pixel_sizes, sigma=2,
size_threshold=100):
39     """
40     Process a TEM image to identify and label particles and convert
measurements to nanometers.
41
42     Parameters:
43     - image_path: Path to the TEM image file.
44     - pixel_sizes: Dictionary of pixel sizes in nanometers per pixel

```

```

    for each image.
45     - sigma: Standard deviation for Gaussian filter.
46     - size_threshold: Minimum size for objects to be considered
particles.
47
48     Returns:
49     - properties_nm: Quantitative properties of the labeled regions
in nanometers.
50     - labeled_image: Image with labeled regions.
51     """
52     # Load the image
53     image = io.imread(image_path)
54     image_name = os.path.basename(image_path)
55     pixel_size_nm = pixel_sizes.get(image_path, None)
56
57     if pixel_size_nm is None:
58         raise ValueError(f"No pixel size found for image {image_path
}.".")
59
60     # Apply a Gaussian filter to smooth the image, which can help in
thresholding
61     smoothed_image = filters.gaussian(image, sigma=sigma)
62
63     # Apply Otsu's method to find an optimal threshold to separate
particles from the background

```

```

64     threshold = filters.threshold_otsu(smoothed_image)
65
66     # Threshold the image
67     binary_image = smoothed_image > threshold
68
69     # Remove small objects (noise) from the binary image
70     cleaned_image = morphology.remove_small_objects(binary_image,
71     min_size=size_threshold)
72
73     # Label the image
74     labeled_image = measure.label(cleaned_image)
75
76     # Measure properties of labeled regions and convert to
77     nanometers
78     properties = measure.regionprops_table(labeled_image,
79     properties=('area', '
80     eccentricity', 'perimeter',
81     major_axis_length', 'minor_axis_length'))
82     properties_nm = {key: (np.array(value) * pixel_size_nm**2 if key
83     == 'area' else np.array(value) * pixel_size_nm)
84     for key, value in properties.items()}
85
86     return properties_nm, labeled_image

```